Engineered NiO/TiO2 and CuO/NiO/TiO2 heterojunctions for sustainable direct photocatalytic epoxidation of propylene using molecular oxygen

Original
Engineered NiO/TiO2 and CuO/NiO/TiO2 heterojunctions for sustainable direct photocatalytic epoxidation of propylene using molecular oxygen / Morante, N., Monzillo, K., Padua, A., Muscatello, A., Sannino, D., Esposito, S., Vaiano, V.. - In: DISCOVER NANO. - ISSN 2731-9229. - 20:1(2025). [10.1186/s11671-025-04296-6]

Availability:
This version is available at: 11583/3002810 since: 2025-09-04T16:49:19Z

Publisher:
Springer

Published
DOI:10.1186/s11671-025-04296-6

Morante *et al. Discover Nano* (2025) 20:104
https://doi.org/10.1186/s11671-025-04296-6

Discover Nano

RESEARCH Open Access

Engineered NiO/TiO_2 and CuO/NiO/TiO_2 heterojunctions for sustainable direct photocatalytic epoxidation of propylene using molecular oxygen

Nicola Morante[1], Katia Monzillo[1], Alessandro Padua[2], Andrea Muscatello[2], Diana Sannino[1], Serena Esposito[2*] and Vincenzo Vaiano[1]

*Correspondence:
Serena Esposito
serena_esposito@polito.it
[1] Department of Industrial Engineering, University of Salerno, Via Giovanni Paolo II 132, 84084 Fisciano, SA, Italy
[2] Department of Applied Science and Technology and INSTM Unit of Turin– Politecnico, Politecnico Di Torino, Corso Duca Degli Abruzzi 24, 10129 Torino, Italy

Abstract

The selective photocatalytic epoxidation of propylene using molecular oxygen under UV-A irradiation presents a promising sustainable alternative for propylene oxide (PO) production. In this study, NiO/TiO_2 and CuO/NiO/TiO_2 heterojunction photocatalysts were synthesized via the thermal annealing of sol-gel-derived TiO_2 and tested in a fluidized bed photoreactor. Structural and optical characterizations confirmed the successful deposition of NiO onto TiO_2 and highlighted the crucial role of NiO content in optimizing charge separation and catalytic efficiency. Among the NiO/TiO_2 series, the NiO(1.1%)/TiO_2 composite exhibited the lowest photoluminescence intensity, indicating reduced electron–hole recombination, while UV–Vis DRS analysis revealed a red shift in the absorption onset and a reduction in the band gap energy. These features resulted in enhanced light absorption and facilitated charge transfer, leading to superior photocatalytic performance compared to lower and higher NiO loadings. Under irradiation, NiO(1.1%)/TiO_2 achieved a propylene conversion of 52.5%, a selectivity to PO of 83.4%, and a PO yield of 43.8%, confirming its effectiveness in promoting selective epoxidation. The introduction of CuO to form the CuO(1.1%)/NiO(1.1%)/TiO_2 heterojunction further enhanced the catalytic performance, reaching 61% propylene conversion, 92% selectivity to PO, and a PO yield of 56%. The improved activity was attributed to the efficient conversion of molecular oxygen into hydrogen peroxide, which acts as a selective oxidant for epoxide formation. Process optimization revealed that water vapor (1000 ppm) significantly enhanced PO selectivity, while incident light intensity played a crucial role in determining conversion rates. The system exhibited excellent stability over 24 h of continuous operation, with no observable deactivation. Furthermore, an energy efficiency analysis demonstrated an exceptionally low energy consumption of 0.019 kWh per mole of propylene converted, significantly outperforming existing photocatalytic systems. These findings highlight the potential of CuO/NiO/TiO_2-based photocatalysts, combined with fluidized bed reactors, as an energy-efficient and scalable approach for sustainable PO production.

Keywords Propylene, Photoepoxidation, Propylene oxide, Photocatalysis, NiO/TiO_2, $CuO/NiO/TiO_2$, Fluidized bed photoreactor

1 Introduction

Propylene oxide (PO) is a crucial chemical intermediate widely utilized in the production of polyurethanes, propylene glycols, and glycol ethers. These derivatives are fundamental in various industrial sectors, including automotive, construction, and textiles, where they are employed in the manufacturing of foams, coatings, adhesives, and other essential materials [1]. With global PO production exceeding 11 million metric tons annually, the need for sustainable and economically viable production methods has become increasingly urgent [2, 3].

Traditionally, PO production has been dominated by the chlorohydrin process and hydroperoxide-based co-oxidation methods, such as the cumene and styrene monomer routes [4]. While these processes are effective, they present significant environmental and economic drawbacks. The chlorohydrin process, which relies on chlorine and lime, generates large quantities of chlorinated byproducts, posing serious environmental disposal challenges and leading to substantial waste management costs [5, 6]. Meanwhile, hydroperoxide-based co-oxidation routes generate co-products such as tert-butyl alcohol or cumene, complicating the separation process and leading to energy inefficiencies. Additionally, these methods often depend on hazardous organic peroxides, raising significant safety concerns related to their handling and storage [7]. In light of these limitations, the research community has increasingly focused on catalytic processes that enable the direct and selective oxidation of propylene to PO. Among these, thermal catalytic methods have been extensively studied. Molybdenum-based catalysts, for instance, have exhibited high selectivity and stability at elevated temperatures. When supported on alumina or silica, these catalysts effectively activate oxygen, promoting selective oxidation reactions by stabilizing reactive oxygen species on their surfaces [8–10]. Recent studies by Šustek et al. 11 and Song et al. 12 have demonstrated that molybdenum-based catalysts can enhance PO yields by improving the interaction between propylene and active oxygen species [11, 12].

Gold-based catalysts, particularly gold nanoparticles, have also shown great promise due to their exceptional ability to activate molecular oxygen at relatively low temperatures. Research indicates that gold nanoparticles supported on titania or mesoporous silica can significantly enhance PO selectivity while minimizing the formation of undesired byproducts [13–15]. Studies by Qi et al. 13 and Hou et al. 14 have demonstrated that gold nanoparticle systems facilitate electron transfer and maintain high PO selectivity, making them effective under mild reaction conditions [13, 14]. In addition, Lin et al. 15 and Xu et al. 16 found that hierarchical zeolites, such as TS-1, offer large surface areas and controlled acidity, which are crucial for suppressing side reactions during propylene epoxidation [15, 16].

Nickel catalysts supported on titanium-silica (Ni/TS-1) have recently shown significant promise, exhibiting high activity and selectivity for propylene epoxidation [17–19]. By utilizing nickel as the active phase, these catalysts provide a cost-effective alternative to traditional gold-based catalysts, achieving comparable selectivity while enhancing the economic sustainability of the process by reducing dependence on expensive noble metals. Li et al. 17 further advanced this field by demonstrating that alkali metal modification of nickel catalysts improves oxygen mobility within the catalyst matrix, thereby enhancing overall catalytic performance [17]. This enhancement not only increases selectivity but also mitigates catalyst deactivation, which is crucial for maintaining long-term catalytic performance. In addition to nickel-based composites, copper-based catalysts have emerged as promising candidates for propylene epoxidation. Notably, copper catalysts exhibit a strong ability to generate reactive oxygen species, effectively facilitating the epoxidation reaction under mild conditions [20–23]. Furthermore, recent research indicates that the performance of copper catalysts can be significantly enhanced through their combination with other metal oxides, particularly ruthenium(IV) oxide (RuO_2), as well as the use of tailored supports and promoters. These advancements lead to improved selectivity and stability, further reinforcing their potential as sustainable alternatives in the epoxidation process [24]. Collectively, these findings underscore the potential of nickel- and copper-based catalysts as economically viable alternatives for sustainable PO production, offering both operational efficiency and cost advantages over conventional noble metal catalysts. Given the environmental and economic challenges associated with traditional methods, green chemistry principles are increasingly shaping the development of PO production processes [25, 26].

Photocatalysis aligns with these principles, providing a green and sustainable alternative for the selective oxidation of propylene to PO under mild conditions. This approach operates at room temperature and atmospheric pressure by leveraging semiconductor activation through light, minimizing energy consumption and reducing environmental impact [27–29]. Additionally, photocatalysis eliminates the need for solvents and significantly reduces the formation of hazardous byproducts, thereby mitigating environmental impact and human health risks [30]. For these reasons, photocatalysis has the potential to reduce energy consumption and simplify downstream separation and purification stages in industrial PO synthesis. Titanium dioxide (TiO_2), one of the most extensively studied photocatalysts, is particularly valued for its low cost, chemical stability, and ability to generate reactive oxygen species upon activation by UV light [31–33].

Nickel oxide (NiO) is a p-type semiconductor with a narrow band gap (~ 3.6–4.0 eV) that exhibits strong redox activity and chemical stability under photocatalytic conditions. When coupled with TiO_2, NiO can act as an efficient hole acceptor, promoting charge separation and suppressing electron–hole recombination, which ultimately enhances photocatalytic activity [34, 35].

Copper oxide (CuO), another p-type semiconductor, possesses a narrower band gap (~ 1.2–1.7 eV) and can absorb visible light, extending the photoresponse range of TiO_2 when used in heterojunctions. CuO also contributes to the generation of reactive oxygen species (ROS) through redox cycling between Cu(I)/Cu(II), which is essential for the activation of molecular oxygen in selective oxidation reactions [36].

When combined, CuO and NiO form binary oxide systems (CuO/NiO) that exhibit synergistic effects in photocatalysis. These effects include enhanced charge separation, broadened light absorption, and improved oxygen activation kinetics. Studies have reported that CuO/NiO heterojunctions coupled semiconductors such as TiO_2, ZnO, or g-C_3N_4 demonstrate significantly improved performance in photocatalytic degradation and selective oxidation reactions, due to the effective alignment of band structures and interfacial charge transfer pathways [37, 38].

Recent advances in heterojunction design have significantly enhanced the performance of TiO_2-based photocatalysts. For instance, NiO/TiO_2 and CuO/TiO_2 heterojunctions have been shown to improve charge separation and minimize electron–hole recombination—key factors in enhancing photocatalytic efficiency [39–42]. Their unique electronic properties, combined with efficient charge transfer mechanisms, provide additional pathways for enhancing photocatalytic activity. This underscores their potential in sustainable chemical processes and positions them as promising catalysts for further research and application in photocatalytic systems.

To further enhance the efficiency of photocatalytic processes, recent scientific studies have focused on the design and synthesis of heterojunctions involving more than two semiconductor oxides. These advanced photocatalysts leverage the synergistic interactions among their three constituent semiconductors, leading to improved separation of photo-excited charge carriers, enhanced generation of reactive oxygen species, and greater selectivity for the desired oxidation or reduction reactions [43–45]. These properties collectively result in a significant enhancement of the overall efficiency and effectiveness of photocatalytic systems.

Additionally, reactor configuration plays a crucial role in optimizing the performance of photocatalytic systems. Fluidized bed reactors offer distinct advantages over fixed-bed reactors, making them particularly suitable for photocatalytic applications. One of their primary benefits is the uniform distribution of the photocatalyst, which enhances light penetration and maximizes photon utilization, leading to improved reaction efficiency [46–48].

They also enhance mass transfer, ensuring rapid reactant delivery and efficient byproduct removal, thereby minimizing catalyst deactivation caused by fouling and coking. Additionally, their effective heat management prevents localized overheating, preserving catalyst integrity and improving long-term performance [46–48]. Moreover, fluidized bed reactors are highly scalable, providing flexibility across operational scales from laboratory research to industrial applications. Additionally, their reduced solvent requirements align with green chemistry principles, further enhancing their sustainability and environmental benefits [46–48].

These combined features contribute to enhanced process efficiency, sustainability, and economic viability, establishing fluidized bed reactors as the preferred configuration for advancing photocatalytic processes.

This study aimed to design, synthesize, and evaluate a titania-based heterojunction incorporating nickel and copper oxides as active phases for the selective photoepoxidation of propylene in a fluidized bed reactor. To our knowledge, this specific combination of materials and reactor configuration has not been previously explored, representing a novel approach in the field of propylene photoepoxidation. This study not only introduces a unique catalyst formulation but also integrates it into an optimized reactor setup, addressing key challenges related to charge separation, oxygen activation, and process scalability. By demonstrating the synergistic effects of TiO_2, NiO, and CuO in the composites within a fluidized bed system, this research offers a promising strategy for enhancing photocatalytic efficiency and selectivity, thereby advancing the development of sustainable and economically viable PO production technologies. These combined features contribute to improved process efficiency, sustainability, and cost-effectiveness, positioning fluidized bed reactors as the preferred configuration for optimizing photocatalytic processes.

2 Materials and methods

2.1 Materials

Titanium tetraisopropoxide ($C_{12}H_{28}O_4Ti$, ≥ 97% w/w, Sigma-Aldrich), copper(II) acetate ($Cu(CO_2CH_3)_2$, ≥ 99% w/w, Sigma-Aldrich), nickel(II) acetate tetrahydrate ($Ni(OCOCH_3)_2 4H_2O$, ≥ 99% w/w, Sigma-Aldrich), distilled water (Carlo Erba), and glass spheres (Lampugnani Sandblasting HI-TECH, 70–110 μm grain size) were purchased and used without further purification.

2.2 Preparation of TiO_2 nanoparticles

The TiO_2 photocatalyst was synthesized using the sol–gel method previously employed in our earlier work, with titanium tetraisopropoxide (TTIP) as the precursor [49]. In this process, 12.5 mL of TTIP was gradually added dropwise to 25 mL of distilled water under continuous stirring at room temperature for 10 min. The resulting suspension was then centrifuged and subjected to three washing cycles with distilled water to remove residual impurities. The purified material was subsequently dried and calcined in a muffle furnace at 450 °C for 30 min under static air conditions.

2.3 Preparation of NiO/TiO_2, and $CuO/NiO/TiO_2$ composites

The photocatalyst samples were prepared via a solid-state reaction to ensure the formation of interfaces between titanium oxide and metal oxides [45–47]. In particular, 3.5 g of pre-synthesized TiO_2 powder, obtained in the previous stage, was thoroughly ground with the metal oxide precursors using an agate pestle and mortar for 3 h. For the NiO(x%)/TiO_2 samples, titanium dioxide was combined with nickel(II) acetate tetrahydrate, where x% denotes the NiO weight percentage in the NiO/TiO_2 composites. For the CuO(1.1%)/TiO_2 sample, titanium dioxide was mixed with copper(II) acetate, with 1.1% representing the optimized CuO weight percentage in the CuO/TiO_2 composite, as determined in our previous work [50]. In the case of the $CuO/NiO/TiO_2$ composite, TiO_2 was ground with a mixture of nickel(II) acetate tetrahydrate and copper(II) acetate, where CuO was fixed at 1.1%, while the NiO content corresponded to the optimized value established from photocatalytic experiments (vide infra).

In addition, pure NiO and pure CuO were synthesized separately by directly calcining nickel(II) acetate tetrahydrate and copper(II) acetate, respectively, under identical conditions.

The resulting finely ground mixtures were then calcined in static air at 400 °C for 2 h in a muffle furnace. This process yielded seven distinct photocatalysts detailed in Table S1.

2.4 Characterization of the photocatalysts

Structural analysis was conducted using powder X-ray diffraction (XRD) on a Philips X'Pert diffractometer. Copper Kα radiation was employed, and the data were collected over a 2θ range of 20°–80°, with a step size of 0.02° and a time per step = 100 s.

Scanning Electron Microscope imaging of the samples was performed with the electron beam column of a dual beam FIB-SEM machine (Solaris X, Tescan, Czech Republic), equipped with an energy dispersive X-ray spectroscopy (EDS) device (UltimMax 40, Oxford Instruments, UK) using a Silicon Drift Detector to acquire EDS spectra from irradiated samples. The EDS detector control software elaborated Elemental maps and compositions (AZtec V. 6.1, Oxford Instruments, UK).

X-ray fluorescence (XRF) analysis was carried out using a Thermo Fisher ARL QUANT'X EDXRF spectrometer to quantify the content of Ni and Cu in the CuO/NiO/TiO_2 composite.

The Brunauer–Emmett–Teller (BET) surface area of the catalysts was determined by dynamic nitrogen adsorption measurements at–196 °C using a Costech Sorptometer 1042. Prior to analysis, the samples underwent a pre-treatment for 30 min in a helium flow at 150 °C.

Raman spectroscopy was performed at room temperature using a Dispersive MicroRaman spectrometer (InVia, Renishaw) equipped with a 514 nm excitation laser, recording spectra over the Raman shift range of 100–1200 cm^{-1}.

UV–Vis diffuse reflectance spectra (UV–Vis DRS) were acquired using a PerkinElmer Lambda 35 spectrophotometer fitted with an RSA-PE-20 reflectance accessory (Labsphere Inc., North Sutton, NH). The band gap values of the composites were calculated using the Kubelka–Munk (K-M) function by plotting $(\text{K-M} \times h\nu)^{0.5}$ against hν, This choice is justified by the indirect allowed nature of the TiO_2 (anatase) band gap [51–53], which governs the overall optical absorption of the heterostructures due to the high dispersion and low loading of the secondary metal oxides. In contrast, for pure CuO and pure NiO, the band gaps were determined using the direct ($n = 2$) and indirect ($n = 0.5$) transition models, respectively, in accordance with their established optical transition types [35, 54].

A Perkin Elmer Spectrofluorometer LS55 was employed to perform fluorescence measurements. For this purpose, an emission spectrum was acquired using an excitation wavelength (λex) of 279 nm and selecting slits of 10 nm. The resulting spectrum was recorded from 375 to 520 nm.

2.5 Photocatalytic tests

Figure 1 presents a schematic representation of the experimental setup used in this study. The system comprises: (i) four Mass Flow Controllers (MFCs) from Brooks Instruments, enabling precise delivery of various chemical species (C_3H_6, O_2, N_2, and H_2O) to the reactor; (ii) a temperature-controlled saturator for supplying vaporized water to the photoreactor; (iii) the photoreactor itself; (iv) a mass spectrometer (Trace MS; ThermoQuest) for analyzing the composition of the gaseous stream exiting the reactor; and (v) a continuous CO–CO_2 analyzer (Uras 14; Hartmann & Braun) for monitoring the concentrations of carbon monoxide and carbon dioxide.

The photoreactor used for the photocatalytic activity tests is a bubbling fluidized bed reactor with a planar geometry. It is equipped with two Pyrex windows to facilitate illumination of the photocatalytic bed, with the light source positioned adjacent to one window to activate the photocatalyst. This reactor design has been utilized in previous photocatalytic studies, and a detailed description can be found in prior publications [48, 55–58]. The light source consists of a matrix of 120 UV-A LEDs (LTPL-C034UVH365) emitting at a peak wavelength of 365 nm. It was designed to optimize the uniformity of light incident (whose values are reported in Figure S1) on the catalyst by employing a

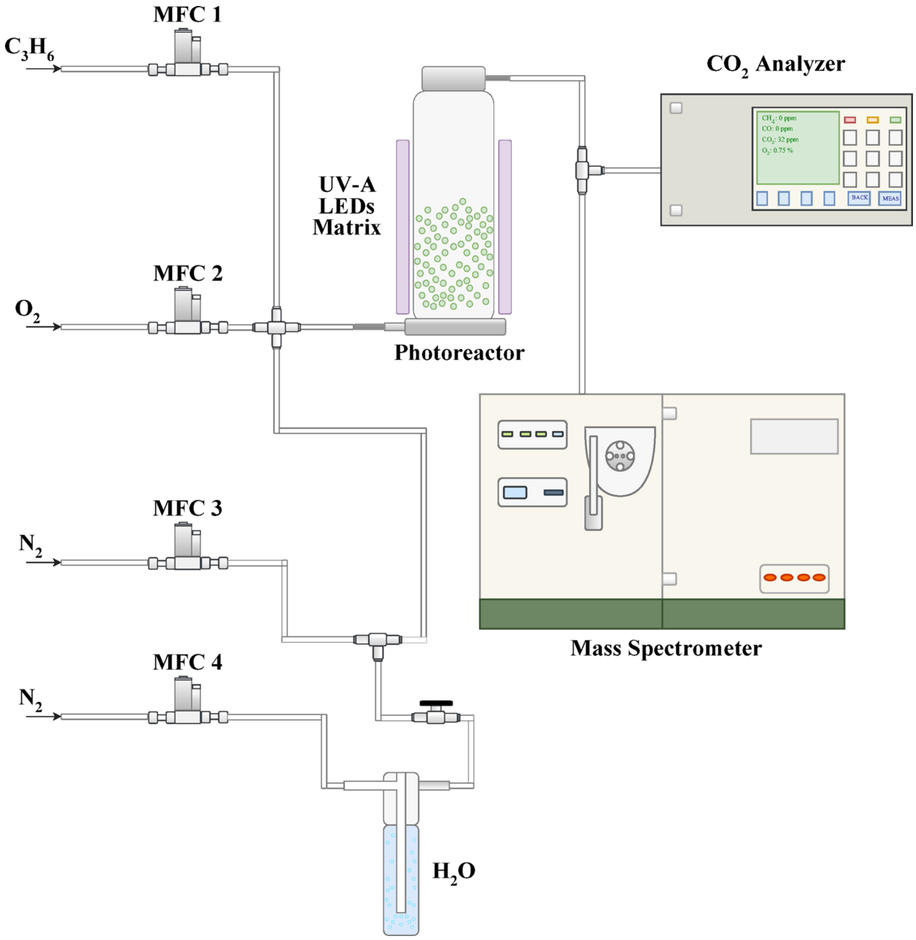

Fig. 1 Experimental setup used for the photoepoxidation tests

triangular arrangement with a reticule spacing of 1.1 cm [59]. A detailed description of the light sources is provided in paragraph SM.1 of the Supporting Information.

Photocatalytic activity tests were conducted using a feed gas mixture of C_3H_6, O_2, H_2O, and N_2, with a total inlet volumetric flow rate of 30 NL h^{-1}. The molar concentrations of propylene and oxygen were maintained at the stoichiometric ratio for the olefin epoxidation reaction ($F_R = C_{C_3H_6}{}^{IN}/C_{O_2}{}^{IN} = 2$), while the concentration of vaporized water in the inlet stream was fixed at 1000 ppm.

Prior to the photoepoxidation experiments, a 3.2 g of the photocatalyst was mixed with 20 g of glass spheres (grain size: 70–110 μm, Lampugnani Sandblasting HI-TECH) to ensure proper fluidization. The mixture was then loaded into the photoreactor. The tests were conducted with the photocatalyst bed operating in a bubbling fluidized regime, maintaining a gas superficial velocity approximately six times higher than the minimum fluidization velocity.

Preliminary experiments were carried out to assess the extent of particle elutriation by fluidizing the powders over several hours. The results indicated no significant particle loss, as corroborated by consistent photocatalytic activity observed throughout the irradiation period during the photoepoxidation tests.

Dark equilibrium adsorption of propylene on the photocatalyst surface was quantified by integrating the concentration profiles obtained prior to the onset of photocatalytic reactions. UV-A LED modules were activated only after complete adsorption of the olefin onto the photocatalyst surface had been confirmed. All photoepoxidation experiments started at ambient temperature, with a subsequent temperature rise to 40 °C following LEDs activation, attributed to heat dissipation from the LEDs. To assess the potential influence of temperature on the photocatalytic performance, a control experiment was conducted in the dark at 40 °C. The test yielded negligible propylene conversion, thereby ruling out any significant contribution from thermal activation. These results confirm that the observed catalytic activity is exclusively attributable to the photocatalytic process.

The data collected during the experiments were used to evaluate the performance of the photocatalytic system. The key parameters analyzed included: (i) propylene conversion (X), (ii) PO yield (Y), (iii) PO selectivity (S), and (iv) CO_x selectivity (SCO_x). These parameters were calculated using the following equations:

$$X = \left(1 - \frac{c_{C_3H_6}^{OUT}}{c_{C_3H_6}^{IN}}\right) * 100 \tag{1}$$

$$Y = \left(\frac{c_{C_3H_6O}^{OUT}}{c_{C_3H_6}^{IN}}\right) * 100 \tag{2}$$

$$S = \left[\frac{c_{C_3H_6O}^{OUT}}{\left(c_{C_3H_6}^{IN} - c_{C_3H_6}^{OUT}\right)}\right] * 100 \tag{3}$$

$$S_{CO_x} = \left[\frac{c_{CO}^{OUT} + c_{CO_2}^{OUT}}{3\left(c_{C_3H_6}^{IN} - c_{C_3H_6}^{OUT}\right)}\right] * 100 \tag{4}$$

where $c_{C_3H_6}^{IN}$ is the inlet concentration of propylene, $c_{C_3H_6}^{OUT}$, $c_{C_3H_6O}^{OUT}$, c_{CO}^{OUT}, and $c_{CO_2}^{OUT}$ are the outlet concentrations of propylene, propylene oxide, carbon monoxide, and carbon dioxide, respectively.

Additionally, two experimental tests were conducted to verify hydrogen peroxide (H_2O_2) generation using the photocatalyst with the optimal NiO loading. In these tests, a feed stream with a flow rate of 30 L h^{-1} (STP), containing either 1000 ppm or 0 ppm water, 1000 ppm oxygen, and nitrogen, was introduced into the reactor. UV-A light was irradiated to activate the photocatalytic bed. The reactor's effluent gas stream was directed into a glass bubbler containing 25 mL of distilled water.

Samples of 1 mL were collected at predefined intervals (0 min, 15 min, 30 min, 60 min, 120 min, 180 min, and 360 min) to determine the presence of H_2O_2. Each sample was treated with 300 μL of titanium(IV) oxysulfate solution, and the absorbance of the resulting $H_2O_2/TiOSO_4$ complex was measured at $\lambda = 410$ nm using a UV–Vis spectrophotometer (Lambda 35, PerkinElmer) [60].

3 Results and discussion

3.1 Photocatalysts characterization

To highlight the structural differences due to the presence of CuO in the NiO/TiO_2 system, the XRD patterns of CuO(1.1%)/TiO_2, NiO(1.1%)/TiO_2 and CuO(1.1%)/NiO(1.1%)/TiO_2 are reported in Fig. 2a. For all samples, the formation of titania in the anatase phase

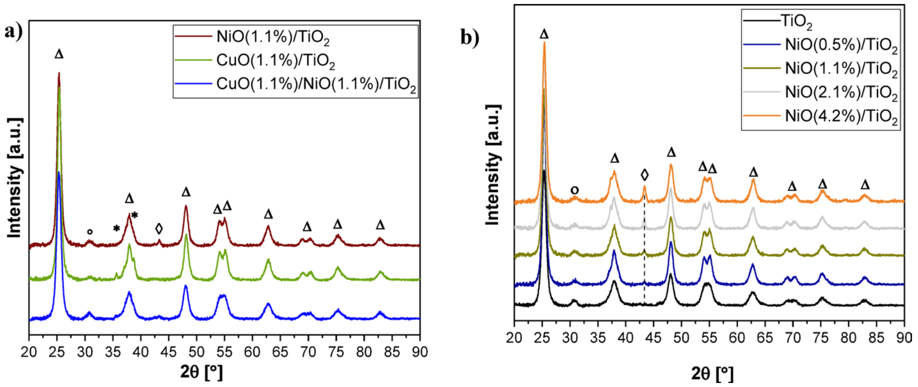

Fig. 2 **a** XRD patterns of CuO(1.1%)/TiO_2, NiO(1.1%)/TiO_2 and CuO(1.1%)/NiO(1.1%)/TiO_2; **b** XRD patterns of NiO(x%)/TiO_2 composites at different NiO loadings, compared with pure TiO_2 spectra. The labels identify the main peaks of anatase (Δ), brookite (°), CuO (*), and NiO (◊)

is confirmed by the presence of characteristic diffraction peaks. In particular, the most intense peaks are observed at 2θ values of 25.36°, 37.94°, 48.09°, 54.13°, and 55.09°, which correspond to the (101), (004), (200), (105), and (211) crystallographic planes, respectively (JCPDS card no. 01-078-2486), with a weak signal at around 30.80° referred to the (121) plane (JCPDS card no. 00-0291360), corresponding to a small amount of brookite, in addition to the typical anatase peaks [45]. The formation of copper oxide is detectable in the CuO(1.1%)/TiO_2 sample, with distinct peaks appearing at 35.5° and 38.9°, which correspond to (– 111) and (200) planes, respectively (CuO JCPDS card no. 00-041-0254). The presence of Cu_2O, if any, is difficult to discern due to the overlap of its most intense peak at 37.11° (JCPDS card no. 35-1091) with one of the anatase peaks of titania. On the other hand, in the NiO sample, a peak at 2θ = 43.30°, assigned to (200), plane due to the formation of NiO is clearly distinguishable (JCPDS card no. 00-004-0835). Surprisingly, in the sample where NiO and CuO coexist with the same content of 1.1%, the signals of the respective oxides are not visible, indicating a synergistic effect that favours their dispersion on the titania matrix. Moreover, a careful analysis of the XRD profiles in Fig. 2a XRD reveals that sample CuO(1.1%)/NiO(1.1%)/TiO_2 exhibits lower crystallinity compared to the single-oxide samples, evidenced by broader, less distinct peaks, particularly the merged doublet at 2θ = 55° and 70°, corresponding to the (211) and (220) planes respectively. Figure 2b shows the XRD patterns of the titania samples with growing nickel content. It is clearly observed that the peak corresponding to the NiO crystallites becomes more easily distinguishable from the background with increasing nickel loading until it is a well-formed peak in the sample NiO(1.1%)/TiO_2.

To investigate the Ni distribution in proximity to the titania surface, scanning electron microscopy (SEM) coupled with energy-dispersive X-ray spectroscopy (EDX) mapping was employed on Cu(1.1%)/NiO(1.1%)/TiO_2, the most performing catalyst for the photocatalytic epoxidation of propylene, as shown in the following section. For comparative analysis, NiO(1.1%)/TiO_2 was also examined to assess the impact of CuO addition on NiO dispersion. SEM image of Cu(1.1%)/NiO(1.1%)/TiO_2 and the relative EDX mapping of Ni, Cu and Ti, are shown in Fig. S2Ia-Id. It revealed a uniform Ni distribution throughout Cu(1.1%)/NiO(1.1%)/TiO_2 sample, indicating no preferential surface localization. Conversely, NiO(1.1%)/TiO_2 (Fig. S2IIa-IId) while displaying a homogeneous Ni distribution, shows significant Ni depletion near the surface.

To complement the qualitative SEM–EDS analysis with quantitative confirmation of metal oxide loading, X-ray fluorescence (XRF) analysis was carried out. Table S2 in Supporting Information presents the elemental and oxide compositions determined for the CuO(1.1%)/NiO(1.1%)/TiO_2 photocatalyst. The XRF results confirm the presence of 0.82 wt% Ni and 0.87 wt% Cu, corresponding to 1.05 wt% NiO and 1.09 wt% CuO, respectively. These findings validate both the target loading values and the successful coupling of the metal oxides with TiO_2, confirming the effective formation of the intended heterojunction system.

Table 1 presents the specific surface area (SSA) values of all photocatalysts, determined using the BET method.

The results indicate that TiO_2 exhibits the highest SSA (79 m^2 g^{-1}), whereas bare NiO and CuO display the lowest values (11 m^2 g^{-1} and 9 m^2 g^{-1}, respectively). For the NiO(x%)/TiO_2 series, the SSA values progressively decrease with increasing NiO content. Specifically, NiO(0.5%)/TiO_2 exhibits an SSA of 78 m2 g^{-1}, closely resembling that of pure TiO_2, indicating minimal surface coverage at this loading. However, as the NiO content increases, the SSA gradually declines, reaching 77 m^2 g^{-1} for NiO(1.1%)/TiO_2, 76 m^2 g^{-1} for NiO(2.1%)/TiO_2, and 75 m^2 g^{-1} for NiO(4.2%)/TiO_2. This inverse correlation between NiO loading and SSA suggests that NiO deposition progressively covers the TiO_2 surface, potentially leading to partial pore blockage and a reduction in available adsorption sites, consistent with trends observed in similar systems reported in the literature [61, 62]. A similar trend is observed for CuO(1.1%)/TiO_2, which has an SSA of 76 m^2 g^{-1}, indicating that CuO deposition also slightly reduces the available surface area. The CuO(1.1%)/NiO(1.1%)/TiO_2 composite exhibits an SSA of 75 m^2 g^{-1}, consistent with the trend of a slight reduction due to the combined presence of both metal oxides. Despite the observed decrease, it is important to note that, in all cases, the reduction in SSA compared to pure TiO_2 is not significant. Even at the highest metal oxide loadings, the SSA values remain within a narrow range, suggesting that the structural integrity of TiO_2 is largely preserved.

The Raman spectra of the NiO(1.1%)/TiO_2, CuO(1.1%)/TiO_2, and CuO(1.1%)/NiO(1.1%)/TiO_2 composite photocatalysts are displayed in Fig. 3a.

The characteristic Raman bands observed at approximately 146, 403, 521, and 640 cm^{-1} correspond to the Eg(1), B1g, A1g + B1g(2), and Eg(2) vibrational modes of anatase TiO_2, respectively [63, 64]. These bands confirm that the anatase phase is preserved after the deposition of metal oxides.

Table 1 Specific surface area (SSA) and optical energy band gap (E_{bg}) values of the synthesized photocatalysts, determined using the BET method and UV–Vis diffuse reflectance spectroscopy, respectively. The data are compared with those of bare NiO and CuO

Sample	*SSA* (m^2 g^{-1})	E_{bg} (eV)
TiO_2	79	3.1
NiO(0.5%)/TiO_2	78	3
NiO(1.1%)/TiO_2	77	2.8
NiO(2.1%)/TiO_2	76	2.75
NiO(4.2%)/TiO_2	75	2.75
CuO(1.1%)/TiO_2	76	3.05
CuO(1.1%)/NiO(1.1%)/TiO_2	75	3
CuO	9	1.5
NiO	11	3.18

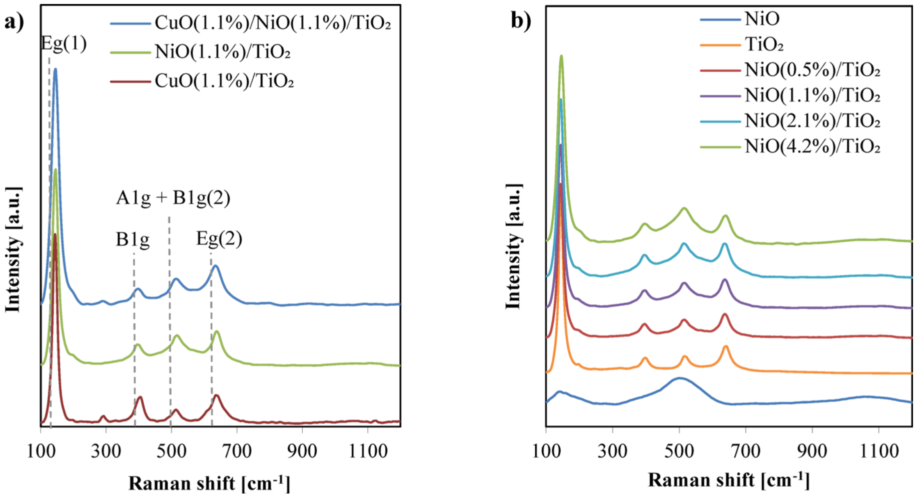

Fig. 3 **a** Raman spectra of CuO(1.1%)/TiO_2, NiO(1.1%)/TiO_2 and CuO(1.1%)/NiO(1.1%)/TiO_2; **b** Raman spectra of NiO(x%)/TiO_2 composites at different NiO loadings, compared with pure TiO_2 and NiO spectra

For the CuO(1.1%)/TiO_2 composite, an additional distinct peak appears at 296 cm^{-1}, which is attributed to the Ag mode of CuO crystals [65]. The presence of this peak confirms the successful deposition of CuO nanoparticles on the TiO_2 surface, forming a CuO/TiO_2 heterojunction. In the case of the NiO(1.1%)/TiO_2 composite, the Raman spectrum shows a slight broadening of TiO_2 bands, particularly in the regions where the E_g and A1g vibrational modes of anatase TiO_2 appear. This effect can be attributed to the influence of NiO, which exhibits its strongest Raman signals at approximately 483 cm^{-1} and 557 cm^{-1}, corresponding to F2g vibrational modes [66–68]. The presence of these features suggests that NiO is well deposited over the TiO_2 surface, interacting with the TiO_2 lattice and slightly modifying its vibrational structure. Furthermore, these intensity variations and spectral broadening effects associated with CuO and NiO deposition are also evident in the Raman spectrum of the CuO(1.1%)/NiO(1.1%)/TiO_2 ternary composite [64, 69]. This confirms the successful deposition of both metal oxides on the TiO_2 surface, leading to heterojunction formation and ensuring efficient interaction between the components.

Figure 3b presents the Raman spectra of the NiO/TiO_2 binary composites at different NiO loadings. With increasing NiO content, a progressive broadening of the characteristic TiO_2 peaks at 396, 517, and 640 cm^{-1} is observed. This trend is primarily associated with the high dispersion of NiO nanoparticles over the TiO_2 surface, which modifies the vibrational structure of the TiO_2 support [68, 70, 71]. For NiO loadings up to 1.1 wt%, the Raman spectra primarily exhibit characteristic TiO_2 bands, with only minor broadening effects. However, for NiO loadings exceeding 1.1 wt%, the TiO_2 bands in the 350–700 cm^{-1} range emerge over a broad underlying signal, which can be attributed to the presence of NiO. This broad feature suggests that, at higher NiO concentrations, NiO forms an extended deposit over the TiO_2 surface, contributing a background signal to the overall spectrum in this Raman shift range. The emergence of this broad signal indicates that NiO begins to form more structured domains at loadings higher than 1.1 wt%. Overall, the interaction between NiO and TiO_2 remains evident across all samples, but the spectral evolution suggests that an optimal NiO loading exists beyond which excessive NiO coverage hinders catalytic efficiency (vide infra).

To investigate the optical properties and estimate the energy band gap of the photocatalysts, UV–visible Diffuse Reflectance Spectroscopy (UV–Vis DRS) was performed (Fig. 4). The Kubelka–Munk (K-M) function was applied to approximate the optical absorbance of the samples, allowing for the determination of their band gap energies [72].

As expected for the anatase polymorph, bare TiO_2 exhibits a steep absorption edge at approximately 385 nm, corresponding to the intrinsic band gap transition. This absorption edge arises from the electronic transition between the valence and conduction bands of TiO_2. Specifically, the valence band is dominated by π bonding orbitals formed by the 3d(t_2g) orbitals of Ti4⁺ ions and the π orbitals of O^{2-} in the TiO_2 crystal lattice, while the conduction band consists of π antibonding orbitals involving the same 3d(t_2g) orbitals in Ti^{4+} ions and O^{2-} orbitals [73].

With increasing NiO content, two notable spectral changes are observed. First, the absorption onset shifts toward longer wavelengths (red shift), indicating that the presence of NiO promotes strong electronic interactions at the NiO/TiO_2 interface. This shift suggests an effective charge transfer transition from the valence band of NiO to the conduction band of TiO_2, extending light absorption into the visible region [73–75]. The most pronounced red shift occurs for NiO(1.1%)/TiO_2, suggesting that this specific NiO loading achieves the most efficient interfacial electronic coupling. For higher NiO loadings (2.1% and 4.2%), the red shift effect diminishes, likely due to the formation of NiO domains, as confirmed by Raman spectroscopy, which could reduce the interfacial charge transfer efficiency. The second key spectral feature is the modification in the

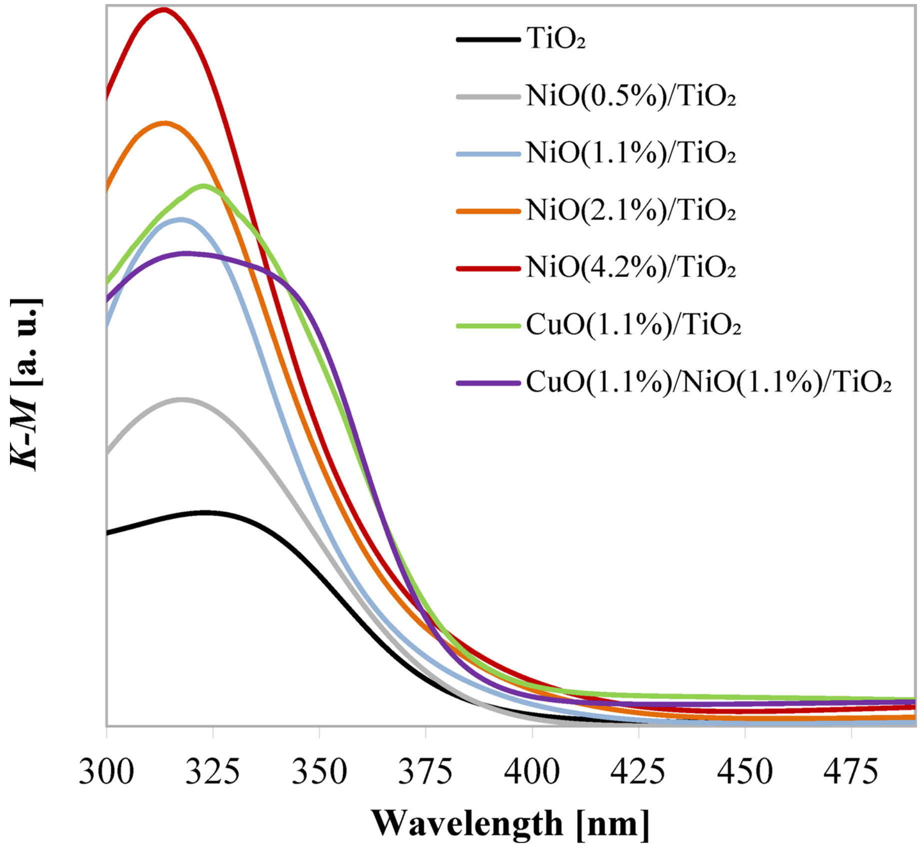

Fig. 4 K-M values as a function of wavelength for the synthesized photocatalysts

position of the absorption maximum in the range 300–350 nm. Compared to pure TiO_2, all NiO-containing samples exhibit a shift in the absorption maximum. However, for NiO(0.5%) and NiO(1.1%), the maximum remains at the same position, indicating that up to this concentration, NiO does not further modify the local electronic states responsible for this transition. When the NiO content exceeds 1.1%, the absorption maximum resumes shifting toward lower wavelengths, suggesting that at higher loadings, NiO begins to influence the optical properties differently, possibly due to changes in particle dispersion or agglomeration effects. These spectral modifications indicate strong electronic interactions between TiO_2 and NiO, but only up to an optimal NiO content [73–75]. A similar trend is observed for CuO(1.1%)/TiO_2 and CuO(1.1%)/NiO(1.1%)/TiO_2, reinforcing the hypothesis of efficient interfacial contact between the deposited oxides and TiO_2, which enhances light absorption and charge carrier dynamics [53, 64, 74–77]. Furthermore, the presence of CuO in the CuO(1.1%)/TiO_2 and CuO(1.1%)/NiO(1.1%)/TiO_2 composites is confirmed by the presence an additional absorption contribution from ~ 340 to ~ 400 nm [64].

To quantitatively assess the evolution of optical properties with increasing NiO content, the band gap energy (E_{bg}) of each NiO/TiO_2 photocatalyst (Table 1) was determined using the Tauc plot method (Figure S3). The results indicate a systematic decrease in band gap energy as NiO content increases. TiO_2 initially exhibits a band gap of 3.10 eV, which gradually reduces upon NiO deposition, reaching 3.00 eV for NiO(0.5%)/TiO_2, 2.80 eV for NiO(1.1%)/TiO_2, and 2.75 eV for both NiO(2.1%)/TiO_2 and NiO(4.2%)/TiO_2. A key observation from these values is that beyond NiO(1.1%), the band gap reduction tends to asymptotically stabilize at ~ 2.75 eV, suggesting that additional NiO loading does not further enhance the electronic coupling with TiO_2. This behavior indicates that there is a saturation point in the modification of the TiO_2 electronic structure, beyond which excess NiO likely forms separate domains rather than continuing to contribute to heterojunction formation. This observation is consistent with the Raman spectra, where NiO domains become evident for loadings above 1.1%, reinforcing the conclusion that NiO(1.1%) represents the optimal composition for maximizing interfacial charge transfer efficiency. A similar band gap reduction is observed for the CuO-containing photocatalysts, with CuO(1.1%)/TiO_2 displaying a band gap of 3.05 eV, while CuO(1.1%)/NiO(1.1%)/TiO_2 reaches 3.00 eV, both values lower than that of bare TiO_2. This trend indicates that CuO and NiO deposition significantly influence the electronic structure of TiO_2, enhancing its optical properties by extending light absorption into the visible range.

To examine how dopants affect the characteristic transitions of TiO_2 anatase, we performed photoluminescence (PL) spectroscopy. Figure 5 shows the PL spectra for the samples under examination. The peak at 425 nm can be attributed to the radiative recombination of self-trapped electrons (STE). This phenomenon occurs when there is the radiative recombination of an exciton, i.e., when an electron with energy greater than or equal to the energy gap can move through the crystal. In this scenario, the electron can be slowed down until it is attracted by a hole through Coulomb forces, thereby generating a quasiparticle known as an exciton. This exciton, upon recombination, leads, in anatase, to the observed 425 nm emission [78]. In contrast, radiative emission at 490 nm indicates an electronic transition from the conduction band to a localized energy level within the band gap, positioned below the Fermi level, generated by oxygen vacancies

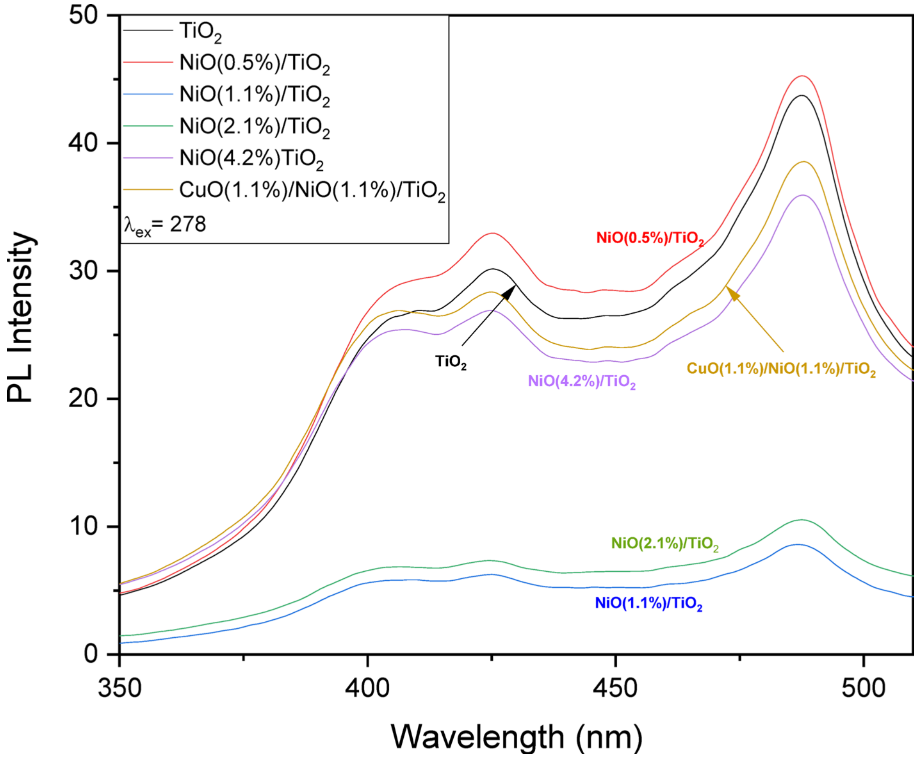

Fig. 5 Photoluminescence spectra of pristine TiO_2 and NiO(x%)/TiO_2 and CuO(1.1%)/NiO(1.1%)/TiO_2 samples

[78]. Therefore, by observing the variation of the intensity of these peaks with nickel content, it can be deduced that these transitions can be hindered and the exciton life prolonged, thus favouring photocatalytic processes. In particular, low NiO doping (0.5%) in TiO_2 has a negligible effect on the optical properties, as evidenced by the emission spectrum in Fig. 5. In contrast, for the samples containing 1.1 and 2.2 weight percent of NiO, a reduction in emission intensity is observed, with the lowest value for NiO(1.1%)/TiO_2. A lower intensity implies more efficient separation of electron–hole pairs, leading to decreased recombination and a positive impact on photocatalytic performance [53]. However, by further increasing the nickel content, the NiO(4.2%)/TiO_2 sample shows an intensity comparable to that of bare TiO_2. This could be caused by several factors, such as the presence of an oxide layer on the surface of TiO_2 (shielding effect) and/or the role of Ni^{2+} as a recombination center [79–81]. Conversely, the CuO(1.1%)/NiO(1.1%)/TiO_2 sample showed no benefit from CuO addition, displaying a spectrum comparable to NiO(4.2%)/TiO_2.

3.2 Photoepoxidation activity tests

3.2.1 Influence of NiO content in NiO(x%)/TiO_2 composite

To evaluate the influence of NiO loading on photocatalytic performance, photoepoxidation experiments were run under controlled conditions, maintaining a stoichiometric molar ratio between propylene and oxygen, and UV-A light intensity of 142 mW cm^{-2}. To assess the effect of NiO loading on the photocatalytic performance, photoepoxidation experiments were conducted under controlled conditions, maintaining a stoichiometric molar ratio between propylene and oxygen and a UV-A light intensity of 142 mW cm^{-2}. The performance of the NiO(1.1%)/TiO_2 catalyst is shown in Fig. 6.

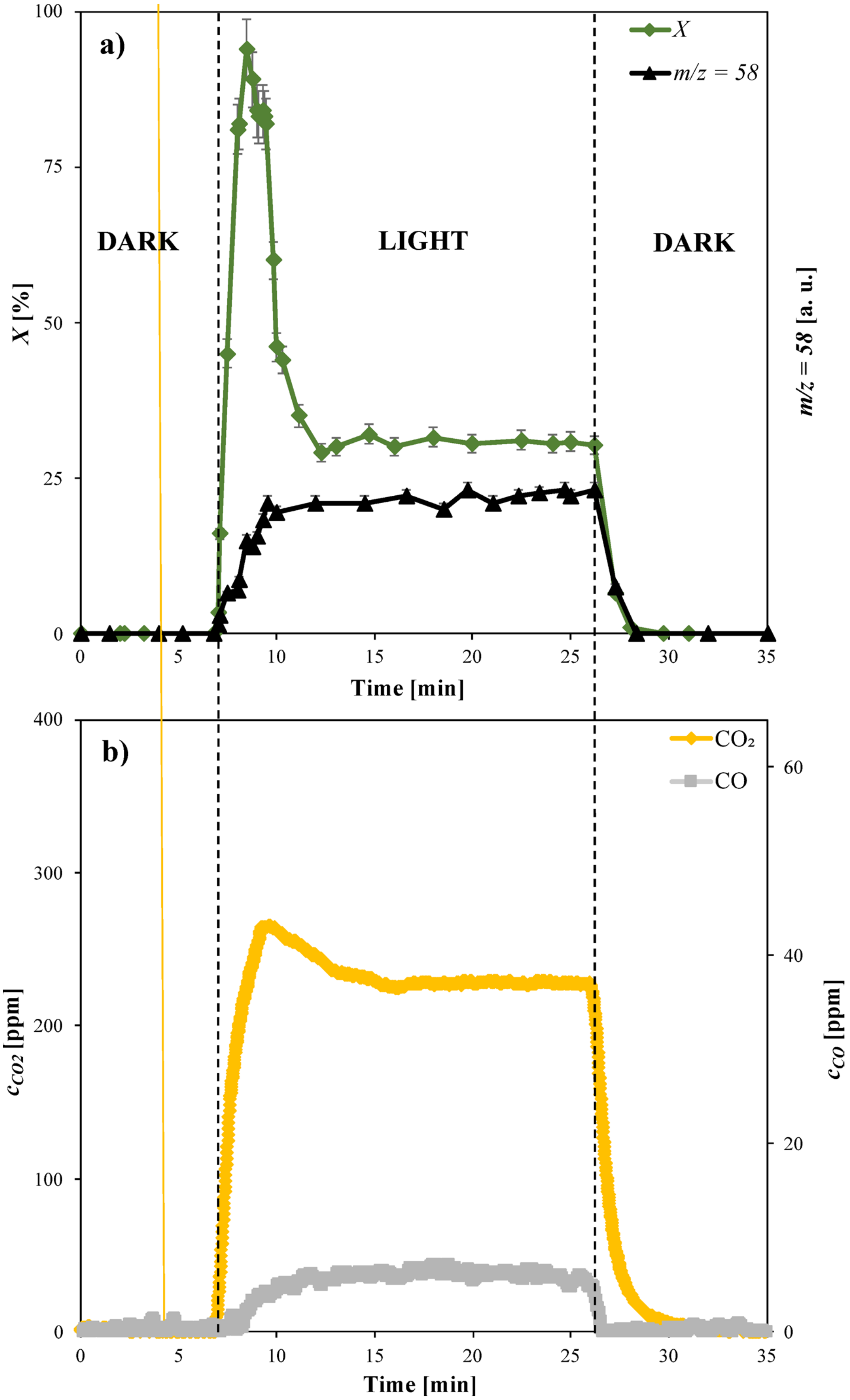

Fig. 6 **a** C_3H_6 conversion (*X*), C_3H_6O concentration, **b** CO_2 and CO concentrations during the photoepoxidation test with NiO(1.1%)/TiO_2 under UV-A light

Upon UV-A irradiation, a sharp increase in C_3H_6 conversion was observed (Fig. 6a), coinciding with a temperature rise from ambient levels to ~ 40 °C, which was induced by LED heating. The conversion rate stabilized within 15 min, indicating the establishment of a steady-state regime.

The initial overshoot in C_3H_6 conversion at the beginning of the light phase, observed before reaching steady-state conditions, can be attributed to the partial desorption of olefin molecules previously adsorbed on the catalyst surface during the dark phase. Upon UV-A activation, these pre-adsorbed species are rapidly released into the gas phase, momentarily increasing the detected conversion rate. Once this desorption contribution is depleted, the system transitions to a purely photocatalytic regime, where the conversion remains stable and governed by photoinduced reaction kinetics. Unlike C_3H_6 conversion, PO generation increased gradually after UV-A activation, without exhibiting a transient peak. The PO concentration progressively rose until reaching a stable value after approximately 20 min, indicating a gradual buildup of PO in the gas phase and confirming the photocatalyst ability to sustain selective epoxidation under continuous irradiation. After switching off the UV-A LEDs, both propylene conversion and PO concentration gradually declined, demonstrating that the reaction is strictly photoinduced with negligible thermal contributions. During irradiation, CO_2 and CO were detected as the only by-products (Fig. 6b), reaching steady-state concentrations of 235 ppm and 6 ppm, respectively. Notably, no other oxygenated by-products were detected, further reinforcing the selectivity of NiO(1.1%)/TiO_2 toward PO formation under these conditions. The same qualitative trend was observed for all the tested photocatalysts.

A comparative summary of the photoepoxidation performance for all tested photocatalysts is presented in Table 2, while Fig. 7 illustrates the trends in PO selectivity (S) and yield (Y) as a function of NiO loading.

The results indicate that bare TiO_2 exhibits low activity, with a propylene conversion of 21.5% and minimal PO selectivity (< 4%), leading to predominant total oxidation (96% selectivity to CO_2 + CO). This behavior reflects the intrinsic limitation of TiO_2, which favors deep oxidation over selective epoxidation due to the lack of a co-catalyst capable of improving charge separation and promoting selective oxygen activation. On the other hand, pure NiO exhibited a very limited propylene adsorption capacity of 0.8 μmol $g_{CAT}{}^{-1}$, consistent with its low specific surface area (11 m2 g^{-1}). As a result, the measured steady-state propylene conversion was only 5.2%, significantly lower than that of TiO_2 (21.5%). Nonetheless, the PO selectivity remained comparable (~ 3.9%), likely reflecting the similar electronic band edge positions of NiO and TiO_2 (vide infra).

Table 2 Steady-state values of propylene adsorption during the dark phase, propylene conversion (X), selectivity (S), and yield to PO (Y), as well as selectivity to CO + CO_2 ($S_{CO\ +\ CO_2}$), for photoepoxidation tests under UV-A light with varying NiO loadings in NiO(x%)/TiO_2 and NiO photocatalysts

Photocatalyst	NiO (wt%)	C_3H_6 Adsorbed (μmol $g_{CAT}{}^{-1}$)	*X* (%)	*S* (%)	*Y* (%)	S_{CO+CO_2} (%)
TiO_2	0	5.5	21.5	3.8	0.8	96.2
NiO(0.5%)/TiO_2	0.5	5.3	24.7	84	20.7	16
NiO(1.1%)/TiO_2	1.1	5.1	33.4	82.4	27.5	17.6
NiO(2.1%)/TiO_2	2.1	4.7	23.2	80.8	18.7	19.2
NiO(4.2%)/TiO_2	4.2	4.5	11.9	77.3	9.2	22.7
NiO	100	0.8	5.2	3.9	0.2	96.1

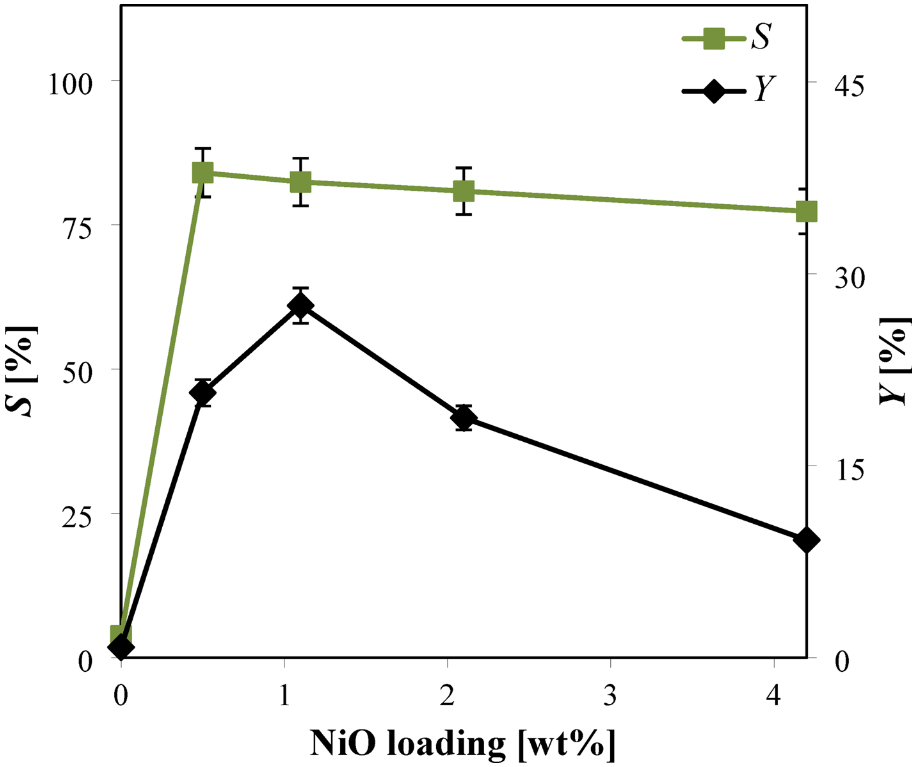

Fig. 7 Steady-state values of selectivity (S) and yield to PO (Y) for photoepoxidation tests under UV-A light as a function of NiO loading in NiO(x%)/TiO_2 photocatalysts

Incorporating NiO into TiO_2 significantly altered the photocatalytic behavior. Increasing the NiO content from 0.5 to 1.1 wt% led to a notable enhancement in both propylene conversion and PO selectivity. The NiO (0.5%)/TiO_2 composite exhibited a propylene conversion of 24.7%, with a PO selectivity of 84.0%, while the NiO (1.1%)/TiO_2 catalyst achieved the highest conversion of 33.4%, along with a selectivity of 82.4% and a PO yield of 27.5%. This improvement can be attributed to multiple factors. First, NiO contributes to the in situ generation of hydrogen peroxide (H_2O_2) from molecular oxygen under UV-A irradiation (vide infra). Since H_2O_2 is a well-known oxidant for epoxidation reactions, its presence enhances the selective oxidation of propylene to PO, aligning with mechanistic pathways reported in the literature [5, 82–84]. Second, the quantity of C_3H_6 adsorbed in dark conditions (Table 2) decreases as NiO content increases, from 5.5 μmol g c_{at}^{-1} for pure TiO_2 to 4.5 μmol g c_{at}^{1} for NiO(4.2%)/TiO_2. The NiO(1.1%)/TiO_{222} composite maintains an adsorption capacity of 5.1 μmol g-c_{at}^{-1}, ensuring a sufficient local concentration of reactants at the catalyst surface. This balance between surface adsorption and reaction kinetics is essential for maximizing PO formation. As the NiO content increased beyond 1.1 wt%, a progressive decline in propylene conversion was observed, dropping to 23.2% for NiO (2.1%)/TiO_2 and further to 11.9% for NiO (4.2%)/TiO_2. This effect can be explained by the shielding effect, where excessive NiO limits TiO_2 activation by absorbing UV photons that would otherwise generate charge carriers in TiO_2 [85–87]. The PL analysis provides additional insight into charge carrier dynamics. The NiO(1.1%)/TiO_2 composite exhibited the lowest PL intensity, indicating a slower recombination rate of photogenerated electrons and holes (Fig. 5). This behavior suggests that NiO at this concentration effectively enhances charge separation by forming a heterojunction with TiO_2, facilitating electron transfer and extending charge carrier lifetimes. In contrast, at higher NiO loadings, PL intensity increased, signaling that excess NiO introduces new recombination centers rather than further improving charge separation. Moreover, Raman spectroscopy (Fig. 3b) confirmed that when the NiO content increased beyond 1.1 wt%, NiO domains start to form. This suggests that at NiO loading higher than 1.1 wt%, phase segregation occurs, reducing the number of interfacial sites where charge transfer can efficiently take place. This structural evolution further supports the decline in catalytic performance beyond 1.1 wt% NiO. Overall, the combined analysis of photocatalytic activity, optical properties, and structural characterization reveals that NiO(1.1%)/TiO_2 exhibits the optimal balance between charge separation, light absorption, and surface reaction dynamics. The enhanced charge separation lead to improved PO formation, while maintaining adequate propylene adsorption ensures a high local reactant concentration. The absence of large NiO clusters at this composition maximizes the NiO/TiO_2 interfacial contact, promoting efficient charge transfer and limiting recombination. Beyond 1.1 wt% NiO, the decline in conversion and yield can be explained by the combined effects of competitive photon absorption, increased charge recombination, and NiO aggregation, all of which reduce the efficiency of the epoxidation reaction. The shielding effect, in particular, reduces TiO_2 activation, while excessive NiO domains disrupt the heterojunction, diminishing its ability to facilitate charge transfer. Therefore, as also illustrated in Fig. 7, the NiO(1.1%)/TiO_2 composite was identified as the optimal photocatalyst, delivering the highest PO yield (27.5%) with high selectivity (82.4%). Based on these findings, the NiO(1.1%)/TiO_2 composite was selected for further investigations, focusing on reaction mechanisms and long-term catalytic stability to validate its applicability in sustainable PO production.

3.2.2 Influence of H_2O presence in the gaseous feed stream and evaluation of in situ H_2O_2 generation under irradiation

To confirm the key the role of in situ H_2O_2 generation in the epoxidation of C_3H_6, photocatalytic tests were conducted using the NiO(1.1%)/TiO_2 catalyst under two different conditions: with and without water in the feed stream. The results, summarized in Table 3, reveal a dramatic shift in reaction selectivity when H_2O is absent from the system. In the absence of H_2O, PO selectivity dropped to zero, while selectivity towards $CO + CO_2$ (S_{CO+CO_2}) increased to nearly 100%. Simultaneously, propylene conversion decreased from 33.4% (with 1000 ppm H_2O) to 10.9%, indicating a significant reduction in overall photocatalytic activity. This decline can be attributed to the absence of hydroxyl radicals (·OH), which are crucial reactive species driving oxidation reactions. Hydroxyl radicals are typically formed through the interaction of photogenerated holes with adsorbed H_2O molecules, and their presence is necessary for both H_2O_2 generation and the oxidation of propylene to PO. Without H_2O, oxidation pathways are dominated

Table 3 Steady-state values of propylene conversion (X), selectivity (S), and yield to PO (Y), as well as selectivity to CO_x(S_{CO+CO_2}), for photoepoxidation tests with the NiO(1.1%)/TiO_2 photocatalyst under UV-A light in the absence and presence of H_2O in the gaseous feed stream

$c^{IN}_{H_2O}$ [ppm]	*X* (%)	*S* (%)	*Y* (%)	S_{CO+CO_2} (%)
0	10.9	n.d	n.d	99.7
1000	33.4	82.4	13.0	28.0

by direct electron transfer mechanisms, leading exclusively to total oxidation products (CO_2 and CO) rather than selective epoxidation [58].

The importance of in situ H_2O_2 formation was further confirmed by analyzing the accumulation of H_2O_2 under UV-A irradiation (Fig. 8).

When 1000 ppm of H_2O was present in the feed, the absorbance signal at 410 nm, corresponding to the H_2O_2–$TiOSO_4$ complex, progressively increased over time, demonstrating continuous in situ H_2O_2 formation during irradiation. In contrast, when H_2O was absent, the signal remained negligible, confirming that no detectable H_2O_2 was produced under dry conditions. These results strongly suggest that the presence of H_2O in the feed stream is essential for enabling H_2O_2-mediated oxidation pathways, which are directly responsible for the selective generation of PO under UV-A irradiation when H_2O is present in the gaseous stream.

3.2.3 Influence of the incident light intensity on the photoepoxidation performance of the NiO(1.1%)/TiO_2 catalyst

The effect of incident light intensity (Φ) on the photoepoxidation activity and selectivity of the NiO(1.1%)/TiO_2 catalyst was systematically analyzed under controlled conditions. Photocatalytic experiments were conducted while varying Φ from 0 to 320 mW cm^{-2}, maintaining constant reactant concentrations of $c_{H_2O} = 1000$ ppm, $c_{C_3H_6} = 4000$ ppm, and $C_{O_2} = 2000$ ppm. The results, summarized in Fig. 9, reveal a linear increase in propylene conversion (X) from 0 to 52.5% as Φ increased from 0 to 297.2 mW cm^{-2} (Fig. 9a). This trend is attributed to the generation of a higher number of photogenerated

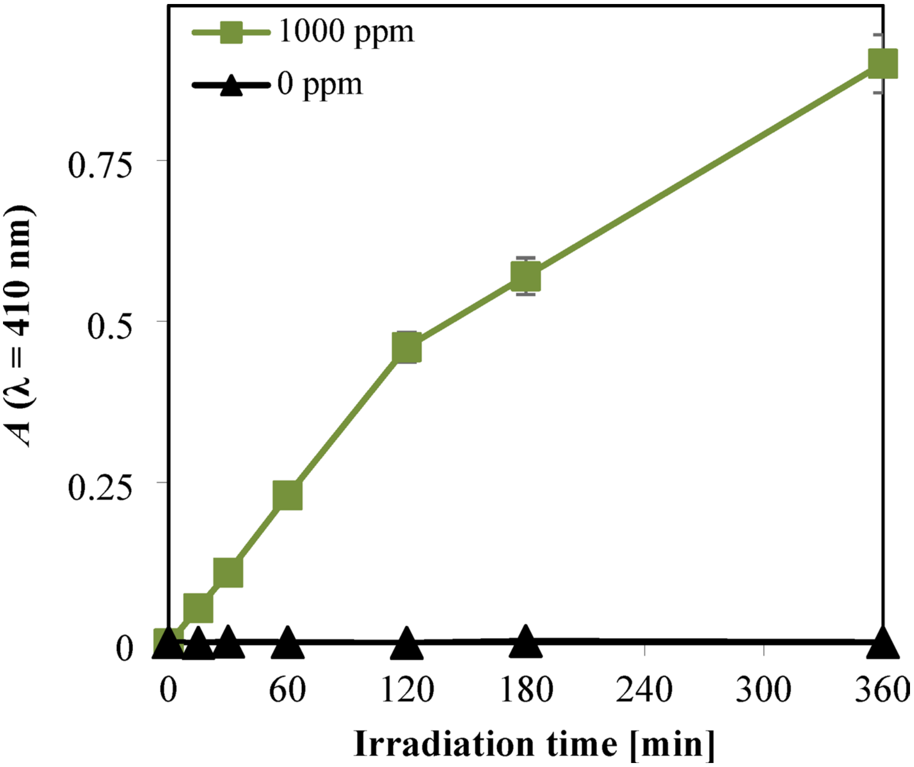

Fig. 8 Absorbance values at 410 nm recorded by UV–Vis spectrophotometer analysis for samples collected during the evaluation of H_2O_2 generation on NiO(1.1%)/TiO_2 under UV-A light light in the absence and presence of H_2O in the gaseous feed stream containing either 1000 ppm or 0 ppm water, 1000 ppm oxygen, and nitrogen

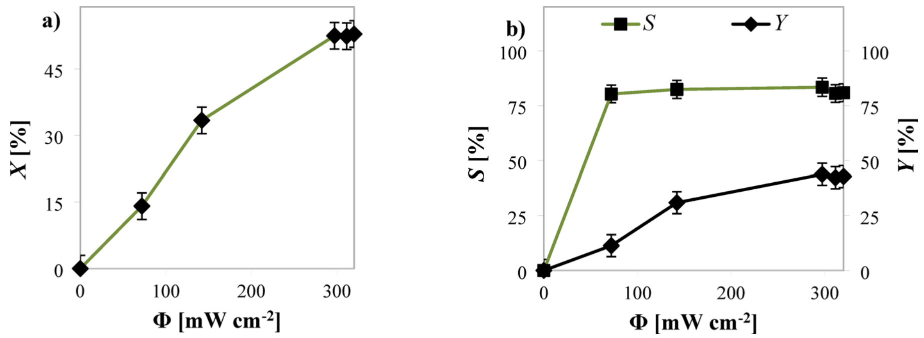

Fig. 9 Steady-state values of **a** propylene conversion (X) and **b** selectivity (S) and yield to PO (Y) for photoepoxidation tests under UV-A light as a function of incident light intensity using the NiO(1.1%)/TiO_2 photocatalyst

electron–hole pairs, which enhances the formation of reactive oxygen species (ROS) and in situ H_2O_2, thereby accelerating the conversion of propylene to PO [88].

At higher light intensities ($\Phi = 297.2–320$ mW cm^{-2}), no further increase in conversion was observed, indicating the onset of a plateau effect. This behavior is likely caused by two factors: (i) enhanced charge carrier recombination at high photon flux, which reduces the number of free charges available for photocatalysis, and (ii) a decline in LED efficiency at maximum power outputs, leading to less effective light utilization [49, 88, 89]. The stabilization of conversion beyond this threshold suggests that the reaction has reached a photon-limited regime, where increasing Φ no longer enhances reaction rates due to intrinsic recombination losses. Despite variations in Φ, the system exhibited stable selectivity, maintaining a value of approximately 81% across all tested light intensities (Fig. 9b). This observation suggests that the mechanism governing selective oxidation remains unchanged, and the ratio between desired and undesired oxidation pathways is not significantly influenced by higher photon fluxes. The maximum PO yield recorded was 43.8% at 297.2 mW cm^{-2}, confirming that this intensity represents the optimal condition for maximizing PO formation.

3.2.4 Influence of propylene inlet concentration on the photoepoxidation performance of the NiO(1.1%)/TiO_2 catalyst

Experimental tests were conducted by varying the propylene concentration in the reactor inlet stream ($c^{IN}_{C_3H_6}$), covering a range from 2000 to 8000 ppm, while maintaining constant H_2O concentration (1000 ppm), oxygen-to-propylene stoichiometric ratio ($\mathrm{F_R} = c^{\mathrm{IN}}_{\mathrm{C_3H_6}} / \mathrm{co_2}^{\mathrm{IN}} = 2$), and light intensity ($\Phi = 297.2$ mW cm^{-2}). The results, summarized in Fig. 10 and Table 4, demonstrate that the reaction system maintained stable selectivity to PO at approximately 83% across all tested conditions, confirming that propylene concentration does not significantly affect the reaction pathway toward selective epoxidation.

Increasing the propylene concentration initially enhanced both conversion and PO yield, highlighting the critical role of propylene availability in facilitating olefin adsorption on the catalyst surface. Within the range of 2000 to 4000 ppm, the increased surface coverage of propylene led to an improvement in conversion (from 48.2 to 52.5%) and PO yield (from 39.2 to 43.8%). This trend suggests that at low-to-moderate $c_{\mathrm{C_3H_6}}$, the active sites on the NiO(1.1%)/TiO_2 photocatalyst effectively adsorb the olefin, promoting efficient oxidation pathways toward PO formation. However, at higher propylene

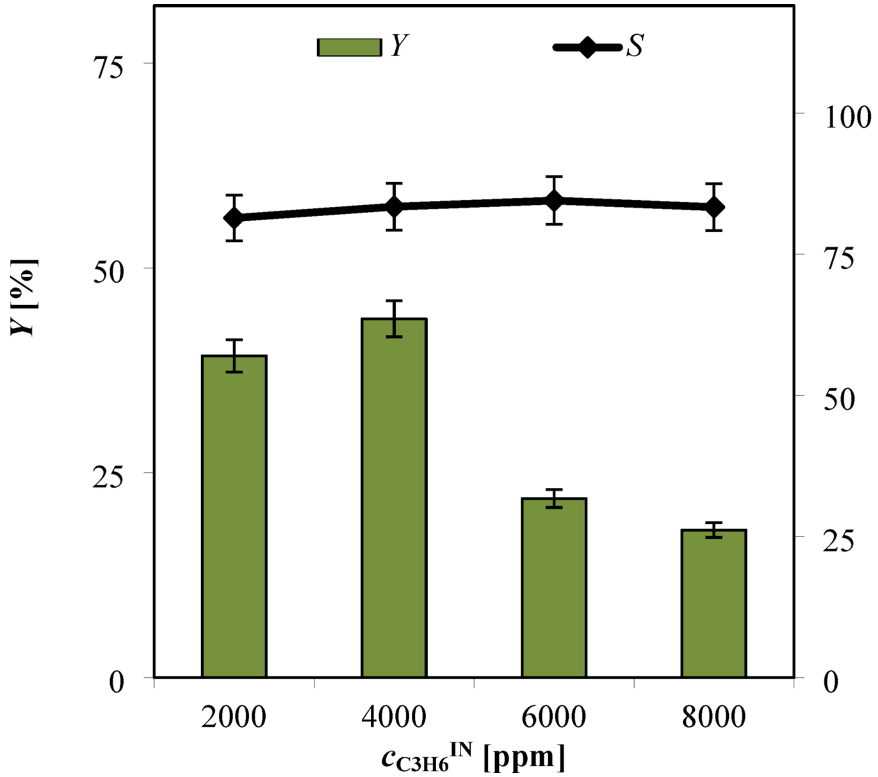

Fig. 10 Steady-state values of selectivity (*S*) and yield to PO (*Y*) for photoepoxidation tests under UV-A light as a function of inlet propylene concentration using the NiO(1.1%)/TiO_2 photocatalyst

Table 4 Steady-state values of propylene adsorption during the dark phase, propylene conversion (X), selectivity (S), and yield to PO (Y), as well as selectivity to CO + CO_2(S_{CO+CO_2}), for photoepoxidation tests under UV-A light as a function of inlet propylene concentration using the NiO(1.1%)/TiO_2 photocatalyst

c_{C3H6}^{IN} [ppm]	C_3H_6 Adsorbed [μmol g_{CAT}^{-1}]	*X* [%]	*S* [%]	*Y* [%]	S_{CO+CO2} [%]
2000	2.6	48.2	81.4	39.2	18.6
4000	5.1	52.5	83.4	43.8	16.6
6000	7.8	25.9	84.5	21.9	15.5
8000	7.7	21.6	83.3	18.0	16.7

concentrations (6000–8000 ppm), a decline in both conversion (down to 21.6%) and PO yield (down to 18.0%) was observed despite the continued increase in adsorption. This decrease can be attributed to competitive adsorption effects, where excess propylene molecules hinder the adsorption of water and oxygen, which are essential for the generation of reactive oxygen ROS and in situ H_2O_2 formation, both necessary for the epoxidation process [90]. Interestingly, the decline in PO yield lessened with further increases in propylene feed concentration, suggesting that the balance of competitive adsorption between propylene, oxygen, and water molecules stabilizes at higher $C_{C_3H_6}^{IN}$ levels. This indicates that while high propylene concentrations inhibit oxidation pathways, the system does not completely shift toward total oxidation, and some degree of PO formation is still maintained.

3.2.5 Photoepoxidation performances of CuO(1.1%)/TiO_2 and CuO(1.1%)/NiO(1.1%)/TiO_2 photocatalysts

The photocatalytic activity of CuO(1.1%)/TiO_2 and CuO(1.1%)/NiO(1.1%)/TiO_2 was evaluated under identical operating conditions (c_{H_2O} = 1000 ppm, $c_{C_3H_6}$ = 4000 ppm, CO_2 = 2000 ppm, and $\Phi = 297.2$ mW cm^{-2}), and the results are summarized in Table 5.

The data indicate that CuO(1.1%)/TiO_2 exhibited moderate activity, achieving a propylene conversion of 31.5% and a PO yield of 22.2%, with a PO selectivity of 70.4%. Compared to NiO(1.1%)/TiO_2, which exhibited a higher conversion (52.5%) and yield (43.8%), the single-metal CuO modification showed reduced performance. This behavior suggests that while CuO enhances photocatalytic activity, it alone does not provide the same charge separation efficiency as NiO, likely due to differences in band alignment and electron transfer dynamics. Additionally, the higher selectivity toward CO_x (29.6%) observed for CuO(1.1%)/TiO_2 suggests that CuO alone may promote partial oxidation pathways, leading to increased CO_2 formation. In contrast, the CuO(1.1%)/NiO(1.1%)/TiO_2 heterojunction demonstrated the highest overall performance, achieving a PO yield of 56.1%, with a propylene conversion of 61.0% and an exceptionally high PO selectivity of 92.0%. The improved activity of the CuO/NiO/TiO_2 system can be attributed to the enhanced interfacial charge transfer (vide infra), where NiO and CuO work cooperatively to facilitate efficient electron–hole separation and oxygen activation [91].

3.2.6 Long-term stability of the CuO(1.1%)/NiO(1.1%)/TiO_2 photocatalyst under continuous UV-A irradiation

The stability of the CuO(1.1%)/NiO(1.1%)/TiO_2 photocatalyst was evaluated through a 24-h irradiation test, performed under the previously determined optimal operating conditions (c_{H_2O} = 1000 ppm, $c_{C_3H_6}$ = 4000 ppm, c_{O_2} = 2000 ppm, and $\Phi = 297.2$ mW cm^{-2}). The results, presented in Fig. 11, demonstrate that both propylene conversion (X) and PO yield (Y) rapidly increased within the first 15 min of irradiation, reaching steady-state conditions. These values remained constant over the entire 24-h reaction period, indicating that no significant deactivation phenomena occurred.

Specifically, steady-state propylene conversion and PO yield were maintained at 61% and 56%, respectively, confirming the excellent long-term stability of the photocatalyst under continuous operation.

Furthermore, post-reaction Raman analysis (Figure S4 in the Supporting Information) revealed no detectable phase transformation in the CuO(1.1%)/NiO(1.1%)/TiO_2 composite, confirming the preservation of its structural integrity after prolonged UV-A irradiation. This stability is particularly important for practical applications, demonstrating that the CuO(1.1%)/NiO(1.1%)/TiO_2 system is a robust and durable photocatalyst for sustained propylene epoxidation under UV-A irradiation.

Table 5 Steady-state values of propylene conversion (*X*), selectivity (*S*) and yield to PO (*Y*), and selectivity to CO + CO_2(S_{CO+CO_2}) for photoepoxidation tests under UV-A light conducted with NiO(1.1%)/TiO_2, CuO(1.1%)/TiO_2 and CuO(1.1%)/NiO(1.1%)/TiO_2

Photocatalyst	*X* (%)	*S* (%)	*Y* (%)	S_{CO+CO_2} (%)
NiO(1.1%)/TiO_2	52.5	83.4	43.79	16.6
CuO(1.1%)/TiO_2	31.5	70.4	22.18	29.6
CuO(1.1%)/NiO(1.1%)/TiO_2	61.0	92.0	56.12	8.0

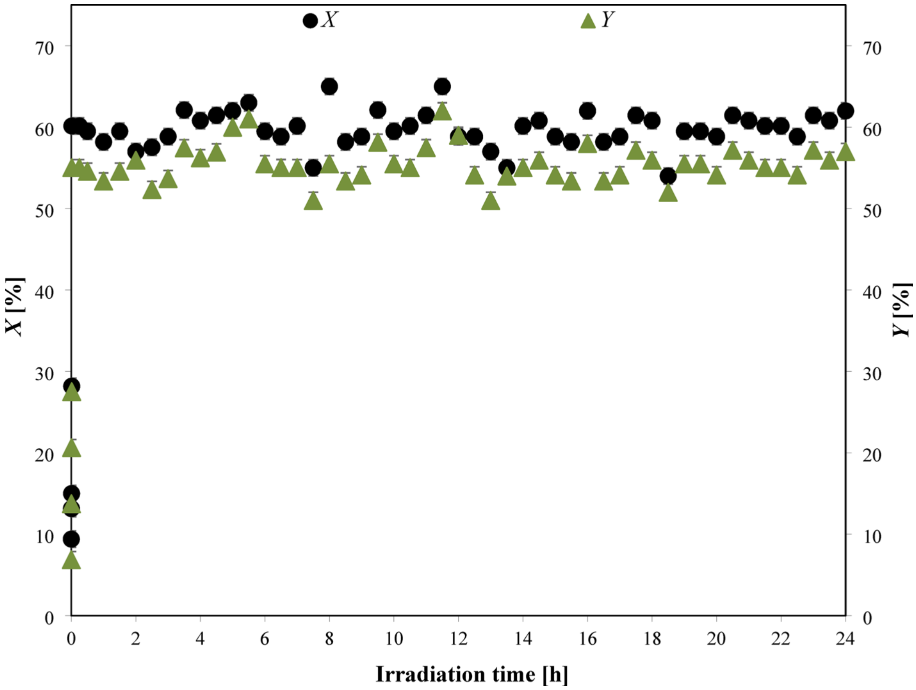

Fig. 11 Propylene conversion (*X*) and yield to PO (*Y*) as a function of irradiation time using the CuO(1.1%)/NiO(1.1%)/TiO_2 photocatalyst (operative conditions: c_{H_2O} = 1000 ppm, $c_{C_3H_6}$ = 4000 ppm, CO_2 = 2000 ppm, and Φ = 297.2 mW cm.$^{-2}$)

3.2.7 Possible reaction mechanisms and charge transfer pathways governing the photoepoxidation of propylene on the CuO(1.1%)/NiO(1.1%)/TiO_2 heterojunction

The band edge positions of the valence band (E_{VB}) and conduction band (E_{CB}) at pH 7 (vs. NHE) for TiO_2, NiO, and CuO were determined using the Mulliken electronegativity method combined with the Nernst equation [38, 92, 93].

$$E_{\mathrm{VB}} = \chi - E_c + \frac{1}{2}E_{bg} - 0.059 * 7 \tag{6}$$

$$E_{\mathrm{CB}} = E_{\mathrm{VB}} - E_{bg} \tag{7}$$

where χ represents the absolute electronegativity of the material, E_c is the energy of free electrons on the hydrogen scale (≈ 4.5 eV), and E_{bg} is the band gap energy derived from UV–Vis DRS analysis. The absolute electronegativity values for TiO_2 (5.81 eV), NiO (5.78 eV), and CuO (5.81 eV) were used, along with their respective band gaps: TiO_2 (3.10 eV), NiO (3.18 eV), and CuO (1.52 eV) [94]. Using these parameters, the calculated EVB/ECB values are + 2.45 V / -0.65 V for TiO_2, + 2.46 V /– 0.72 V for NiO, and + 1.66 V/ + 0.14 V for CuO (vs. NHE at pH 7). These values define the band alignment depicted in Fig. 12, confirming that the NiO/CuO/TiO_2 heterojunction exhibits a type I (straddling gap) configuration [95]. The assumption of pH = 7 was adopted for consistency with the Mulliken electronegativity method, as is commonly reported in the literature for gas-phase photocatalytic systems [50, 96].

Upon UV-A irradiation, the CuO(1.1%)/NiO(1.1%)/TiO_2 composite efficiently absorbs light, generating photoexcited electron–hole pairs. The photogenerated holes from the NiO valence band (VB) migrate to the TiO_2 VB, and subsequently transfer to the CuO VB. Meanwhile, electrons excited in the NiO conduction band (CB) are transferred to

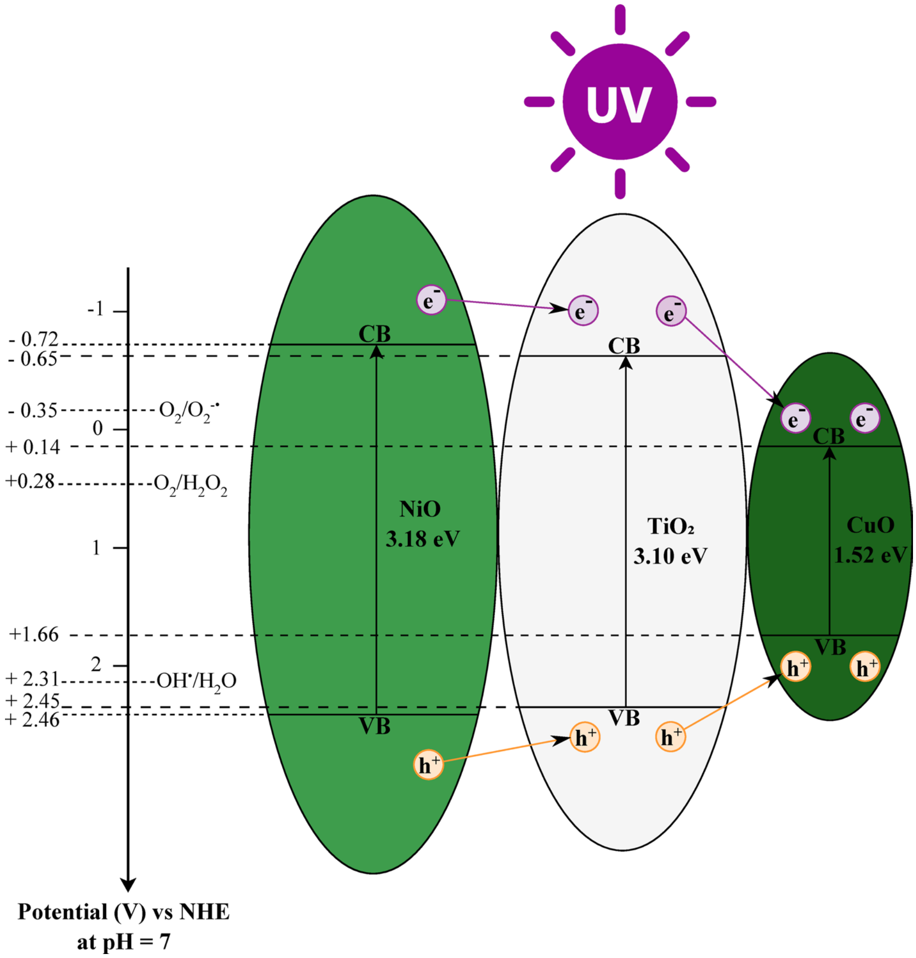

Fig. 12 Proposed mechanism for electron and hole transfer for CuO(1.1%)/NiO(1.1%)/TiO_2 composite in propylene photoepoxidation under UV-A light irradiation

the TiO_2 CB, and finally reach the CuO CB. This directional charge migration is driven by the band alignment of the heterojunction, which facilitates efficient charge separation and minimizes recombination losses.

Since the $O_2/O_2{\cdot}^-$ redox potential (– 0.35 V vs. NHE at pH 7) [87] is more negative than the E_{CB} of CuO (+0.14 V vs. NHE), electrons in the CuO CB cannot reduce molecular oxygen to superoxide ($O_2{\cdot}^-$). However, as the E_{CB} of CuO is less positive than the O_2/H_2O_2 redox potential (+0.28 V vs. NHE) [97], electrons in the CuO CB can promote the reduction of O_2 to H_2O_2 via proton-coupled electron transfer, a process enhanced by proton hopping and diffusion [98]. This pathway ensures the formation of H_2O_2, which plays a crucial role in the selective oxidation of propylene to PO. In regions where TiO_2 is not directly in contact with CuO and NiO, the holes in the TiO_2 VB oxidize adsorbed H_2O, generating hydroxyl radicals (·OH). This oxidation process is thermodynamically favorable, as the $OH{\cdot}/H_2O$ redox potential (+2.31 V vs. NHE) [97] is less positive than the E_{VB} of TiO_2 (+2.45 V vs. NHE). In contrast, holes in the CuO VB cannot oxidize water, as the E_{VB} of CuO (+1.66 V vs. NHE) is less positive than the $OH{\cdot}/H_2O$ redox potential, making CuO ineffective for direct water oxidation.

Based on these findings, the proposed reaction mechanism involves multiple steps.

$$\mathrm{CuO\,(1.1\%)\,/NiO\,(1.1\%)\,/TiO_2 + h\nu \rightarrow h^+ + e^-} \tag{8}$$

$$\mathrm{h^+ + H_2O}_{(ads)} \rightarrow \ \mathrm{OH^{\cdot} + H^+} \tag{9}$$

$$\mathrm{2e^- + O_2 + 2H^+ \rightarrow H_2O_2} \tag{10}$$

$$\mathrm{C_3H_6}_{(ads)} + \mathrm{H_2O_2 \rightarrow C_3H_6O\ + H_2O} \tag{11}$$

$$\mathrm{C_3H_6}_{(ads)} + \mathrm{OH^{\cdot}/h^+} \rightarrow \ \text{intermediates} \ \rightarrow \ \mathrm{CO_2 + \ H_2O} \tag{12}$$

First, upon UV-A irradiation, charge separation occurs according to the Eq. 8. The holes in the TiO_2 VB oxidize adsorbed water, forming hydroxyl radicals (Eq. 9). Simultaneously, the electrons in the CuO CB reduce molecular oxygen to hydrogen peroxide (Eq. 10). The formed H_2O_2 serves as the primary oxidant for the selective epoxidation of adsorbed propylene, leading to PO formation (Eq. 11). A secondary pathway involves propylene oxidation via hydroxyl radicals and photogenerated holes, resulting in CO_2 formation (Eq. 12). This mechanism highlights the synergistic role of CuO, NiO, and TiO_2 in promoting efficient charge separation, enhancing oxygen activation, and driving selective PO formation. The dual metal oxide heterojunction facilitates the formation of H_2O_2 as a key oxidant, while minimizing electron–hole recombination and undesired deep oxidation to CO_2. This pathway is consistent with the high PO selectivity (92%) and enhanced photocatalytic efficiency observed for the CuO(1.1%)/NiO(1.1%)/TiO_2 composite, validating its superior performance in propylene photoepoxidation.

3.2.8 *Electric energy consumption and comparison with the literature*

The photocatalytic test data enabled the calculation of the electric energy required to convert one mole of propylene (E_M) using the empirical equation developed by Bolton et al. [99], as expressed by:

$$E_{\mathrm{M}} = \frac{P}{F_{\mathrm{C_3H_6}}^{\mathrm{IN}} X} \tag{13}$$

where P represents the nominal power of the light source (kW), $F_{\mathrm{C_3H_6}}^{\mathrm{IN}}$ is the molar flow rate of propylene in the inlet stream ($\mathrm{mol_{C_3H_6}h^{-1}}$), and X denotes the propylene conversion.

A comparative analysis of photocatalytic propylene epoxidation systems from the literature was conducted, focusing on operating parameters, photocatalyst types, and energy consumption values, as summarized in Table 6.

The results reveal that the fluidized bed reactor (FBPR) configuration used in this study offers a distinct advantage over conventional fixed-bed photocatalytic reactors (PBPRs), particularly in terms of lower energy consumption as well as higher conversion and yield.

Among the reported photocatalytic systems, our optimized CuO(1.1%)/NiO(1.1%)/TiO_2 photocatalyst exhibited the lowest E_M value (0.019 kWh $\mathrm{mol^{-1}_{C_3H_6\ conv}}$), significantly outperforming other photocatalytic systems. The results emphasize that the CuO(1.1%)/NiO(1.1%)/TiO_2 heterojunction is a highly promising photocatalyst for energy-efficient and selective propylene epoxidation, providing a sustainable alternative to conventional catalytic processes.

Table 6 Comparison with literature works dealing with different photocatalysts for propylene Epoxidation under UV-A light. PBPR = fixed bed photocatalytic reactor; FBPR = fluidized bed photocatalytic reactor

Photocatalyst	Type of reactor	$F^{\mathrm{IN}}_{\mathrm{C_3H_6}}$(mol h^{-1})	X (%)	Y (%)	P [kW]	E_M (kW h $\mathrm{mol}^{-1}_{\mathrm{C_3H_6conv}}$)	Refs
V0.2/MCM-41	PBPR	2.65	0.07	0.07	0.2	107.80	[100]
V0.2Ti0.3/MCM-41	PBPR	2.65	0.16	0.16	0.2	47.20	[100]
Ti0.3/MCM-41	PBPR	2.65	0.01	0.01	0.2	754.70	[100]
Rb ion-modified 1.5% (wt) V2O5/SiO2	PBPR	0.011	1.56	1.60	0.3	1748.20	[101]
TiO_2	PBPR	0.01	5.5	5.50	4.3	7818.20	[102]
ZrO_2	PBPR	0.01	5	5	6.3	12,600.00	[102]
BiWO-Ti50i/Glass Spheres	FBPR	5.4	10	10	0.1	0.19	[103]
CuO(1.1%)/NiO(1.1%)/TiO_2	FBPR	5.4	61	56.12	0.057	0.019	Our Optimal Test

4 Conclusions

This study investigated the selective photocatalytic epoxidation of propylene under UV-A irradiation using NiO/TiO_2 and CuO/NiO/TiO_2 heterojunction photocatalysts in a fluidized bed photoreactor. Structural, morphological, and optical characterizations confirmed the successful deposition of NiO and CuO onto TiO_2, leading to enhanced charge separation and reduced electron–hole recombination. Among the NiO/TiO_2 series, NiO(1.1%)/TiO_2 exhibited the best performance, achieving 52.5% propylene conversion, 83.4% selectivity to PO, and a PO yield of 43.8%. The improved activity was attributed to optimized charge transfer dynamics, a reduction in the band gap energy, and the enhanced generation of hydrogen peroxide, which plays a key role in selective epoxidation. Further modification with CuO led to the development of the CuO(1.1%)/NiO(1.1%)/TiO_2 heterojunction, which significantly enhanced photocatalytic efficiency. This system achieved 61% propylene conversion, 92% selectivity to PO, and a PO yield of 56%, making it the most effective catalyst tested. The improved performance was ascribed to the synergistic interaction between CuO and NiO, which facilitated charge migration, reduced recombination losses, and promoted oxygen activation into H_2O_2, a key oxidant for the selective epoxidation of propylene. Process optimization demonstrated that water vapor (1000 ppm) played a crucial role in enhancing PO selectivity by promoting in situ H_2O_2 formation, while incident light intensity strongly influenced conversion efficiency. Stability tests confirmed that the CuO(1.1%)/NiO(1.1%)/TiO_2 photocatalyst remained highly stable over 24 h of continuous operation, with no observable deactivation. Additionally, an energy consumption analysis revealed an exceptionally low energy requirement of 0.019 kWh per mole of propylene converted, highlighting the superior efficiency of the proposed system compared to conventional photocatalysts reported in the literature.

These findings underscore the potential of CuO/NiO/TiO_2 heterojunctions in combination with fluidized bed photoreactors as a viable, scalable, and energy-efficient approach for sustainable propylene oxide production.

Supplementary Information

The online version contains supplementary material available at https://doi.org/10.1186/s11671-025-04296-6.

Supplementary Material 1.

Author contributions

Conceptualization, V.V. and S.E.; methodology, V.V. and S.E.; data curation, N.M and K.M.; formal analysis, K.M., A.M and A.P. writing—original draft preparation, N.M.; writing—review and editing, V.V. and S.E.; visualization, D.S.; supervision, V.V. and S.E. All authors have read and agreed to the published version of the manuscript.

Funding
No funding was received.

Availability of data and materials

Ethics, Consent to Participate, and Consent to Publish declarations: not applicable.

Declarations

Ethics approval and consent to participate

Not applicable.

Consent to publish

Not applicable.

Competing Interests

The authors declare no competing interests.

Received: 9 April 2025 / Accepted: 23 June 2025

References

1. Chi M, Ke J, Liu Y, Wei M, Li H, Zhao J, Zhou Y, Gu Z, Geng Z, Zeng J. Spatial decoupling of bromide-mediated process boosts propylene oxide electrosynthesis. Nat Commun. 2024. https://doi.org/10.1038/s41467-024-48070-1.
2. Alvear M, Schmidt C, Reinsdorf O, Lebron-Rodrigez E, Al Abdulghani A, Hermans I, Peurla M, Lastusaari M, Eränen K, Murzin DY, Kumar N, Salmi T. Ti-MWW Catalysts for Propylene Oxide Production: Influence of Si/Ti Ratio and Calcination Conditions. Catal Letters. 2024;154:834–45. https://doi.org/10.1007/s10562-023-04350-x.
3. Ditthawat N, Pornmai K, Santikunaporn M, Kungsanant S, Meeyoo V, Chavadej S. Propylene epoxidation in a low-temperature parallel-plate dielectric barrier discharge reactor with two frosted glass plates: effects of separate propylene feed. Plasma Chem Plasma Process. 2024;44:907–25.
4. Nijhuis TA, Makkee M, Moulijn JA, Weckhuysen BM. The production of propene oxide: Catalytic processes and recent developments. Ind Eng Chem Res. 2006;45:3447–59.
5. Alvear M, Fortunato M, Eränen K, Lehtonen J, Rautiainen S, Di Serio M, Russo V, Salmi T. Epoxidation of light olefin mixtures with hydrogen peroxide on TS-1 Catalyst. Catal Letters. 2024;154:2101–11. https://doi.org/10.1007/s10562-023-04459-z.
6. Russo V, Tesser R, Santacesaria E, Di Serio M. Chemical and technical aspects of propene oxide production via hydrogen peroxide (HPPO process). Ind Eng Chem Res. 2013;52:1168–78.
7. Meng Y, Taddeo F, Aguilera AF, Cai X, Russo V, Tolvanen P, Leveneur S. The lord of the chemical rings: Catalytic synthesis of important industrial epoxide compounds. Catalysts 11 (2021)
8. Kargar H, Centore R, Fallah-Mehrjardi M, Santagata E, Munawar KS. Dihalosalicylaldehyde based molybdenum(VI) complexes: synthesis, spectral characterization, crystal structures, and catalytic activities for the selective oxidation of benzylic alcohols. Inorganica Chim Acta. 2024. https://doi.org/10.1016/j.ica.2024.122015.
9. Yu X, Xiong C, Liang Y, Zhou X, Xue C. Construction of a highly stable natural silicate-supported molybdenum catalyst for efficient epoxidation of olefins. J Colloid Interface Sci. 2024;660:490–501. https://doi.org/10.1016/j.jcis.2024.01.117.
10. Gomes DM, Yao X, Neves P, Pinna N, Russo PA, Valente AA. Bulky olefin epoxidation under mild conditions over Mo-based oxide catalysts. Catal Sci Technol. 2024;14:646–59. https://doi.org/10.1039/d3cy01299a.
11. Šustek M, Horváth B, Vávra I, Gál M, Dobročka E, Hronec M. Effects of structures of molybdenum catalysts on selectivity in gas-phase propylene oxidation. Cuihua Xuebao/Chinese J Catalysis. 2015;36:1900–9. https://doi.org/10.1016/S1872-2067(15)60961-5.
12. Song Z, Mimura N, Bravo-Suárez JJ, Akita T, Tsubota S, Oyama ST. Gas-phase epoxidation of propylene through radicals generated by silica-supported molybdenum oxide. Appl Catal A Gen. 2007;316:142–51. https://doi.org/10.1016/j.apcata.2006.08.029.
13. Qi C, Cheng Y, Yang Z, Ishida T, Su H, Zhang J, Sun X, Sun L, Zhao L, Murayama T. Efficient formation of propylene oxide under low hydrogen concentration in propylene epoxidation over Au nanoparticles supported on V-doped TS-1. J Catal. 2024. https://doi.org/10.1016/j.jcat.2024.115608.
14. Hou L, Yan S, Liu L, Liu J, Xiong G. Fabrication of gold nanoparticles supported on hollow microsphere of nanosized TS-1 for the epoxidation of propylene with H2 and O2. Chem Eng J. 2024. https://doi.org/10.1016/j.cej.2024.148676.
15. Lin D, Xu Y, Zheng X, Sheng W, Liu Z, Yan Y, Cao Y, Liu Y, Feng X, Chen D, Yang C. Engineering sodium-decorated bifunctional Au-Ti sites to boost molecular transfer for propene epoxidation with H2 and O2. AIChE J. 2023. https://doi.org/10.1002/aic.17999.
16. Xu J, Zhang Z, Yu D, Du W, Song N, Duan X, Zhou X. Au/TS-1 catalyst for propylene epoxidation with H2 and O2: Effect of surface property and morphology of TS-1 zeolite. Nano Res. 2023;16:6278–89. https://doi.org/10.1007/s12274-023-5440-5.
17. Li W, Li W, Cao X, Chen L, Qin Y, Zhu Y, Zhang Y, Miao G, Kong L, Li J, Chen X. Efficient epoxidation of propylene over non-noble nickel-based catalyst promoted by alkali metals. Sci China Chem. 2024. https://doi.org/10.1007/s11426-024-2161-9.

18. García-Aguilar J, Fernández-Catalá J, Juan-Juan J, Such-Basáñez I, Chinchilla LE, Calvino-Gámez JJ, Cazorla-Amorós D, Berenguer-Murcia,. Novelty without nobility: Outstanding Ni/Ti-SiO2 catalysts for propylene epoxidation. J Catal. 2020;386:94–105.
19. Li W, Chen L, Qiu M, Li W, Zhang Y, Zhu Y, Li J, Chen X. Highly Efficient epoxidation of propylene with in situ-generated H2O2 over a hierarchical TS-1 zeolite-supported non-noble nickel catalyst. ACS Catal. 2023;13:10487–99. https://doi.org/10.1021/acscatal.3c02206.
20. Vaughan OPH, Kyriakou G, MacLeod N, Tikhov M, Lambert RM. Copper as a selective catalyst for the epoxidation of propene. J Catal. 2005;236:401–4. https://doi.org/10.1016/j.jcat.2005.10.019.
21. Wang Y, Chu H, Zhu W, Zhang Q. Copper-based efficient catalysts for propylene epoxidation by molecular oxygen. Catal Today. 2008;131:496–504. https://doi.org/10.1016/j.cattod.2007.10.022.
22. Diekmann M, Koch G, König M, Ressler T. Correlation between copper oxide particle size and selectivity towards propylene oxide in selective oxidation of propene. ChemCatChem. 2018;10:5459–67. https://doi.org/10.1002/cctc.201801369.
23. Teržan J, Huš M, Likozar B, Djinović P. Propylene epoxidation using molecular oxygen over copper-and silver-based catalysts: a review. ACS Catal. 2020;10:13415–36.
24. Seubsai A, Uppala C, Tiencharoenwong P, Chukeaw T, Chareonpanich M, Zohour B, Noon D, Senkan S. High stability of ruthenium–copper-based catalysts for epoxidation of propylene. Catal Letters. 2018;148:586–600. https://doi.org/10.1007/s10562-017-2262-7.
25. Schaub T. Efficient industrial organic synthesis and the principles of green chemistry. Chem Eur J. 2021;27:1865–9.
26. Anastas P, Eghbali N. Green chemistry: principles and practice. Chem Soc Rev. 2010;39:301–12. https://doi.org/10.1039/b918763b.
27. Bhattacharjee J, Roy S. A review on photocatalysis and nanocatalysts for advanced organic synthesis. Hybrid Advances. 2024;6: 100268. https://doi.org/10.1016/j.hybadv.2024.100268.
28. Quintavalla A, Carboni D, Lombardo M. Green metrics and sustainability in photocatalysis. ChemCatChem 16 (2024)
29. Wang Y, Yang Y, Deng Q, Chen W, Zhang Y, Zhou Y, Zou Z. Recent Progress of Amorphous Porous Organic Polymers as Heterogeneous Photocatalysts for Organic Synthesis. Adv Funct Mater 33 (2023)
30. Wang Y, Liu XF, He WM. Recent advances in the photocatalytic synthesis of aldehydes. Organic Chem Front. 2023;10:4198–210.
31. Tu JL, Huang B. Titanium in photocatalytic organic transformations: current applications and future developments. Org Biomol Chem. 2024;22:6650–64.
32. Wang J, Wang Z, Wang W, Wang Y, Hu X, Liu J, Gong X, Miao W, Ding L, Li X, Tang J. Synthesis, modification and application of titanium dioxide nanoparticles: a review. Nanoscale (2022)
33. Oi LE, Choo MY, Lee HV, Ong HC, Hamid SBA, Juan JC. Recent advances of titanium dioxide (TiO2) for green organic synthesis. RSC Adv. 2016;6:108741–54.
34. Chen X, Mao SS. Titanium dioxide nanomaterials: synthesis, properties, modifications and applications. Chem Rev. 2007;107:2891–959.
35. Ramasamy R, Ramachandran K, Philip GG, Ramachandran R, Therese HA, Gnana Kumar G. Design and development of Co3O4/NiO composite nanofibers for the application of highly sensitive and selective non-enzymatic glucose sensors. RSC Adv. 2015;5:76538–47. https://doi.org/10.1039/c5ra11739a.
36. Koohestani H, Ezoji R. Synthesis and characterization of TiO2/CuO/WO3 ternary composite and its application as photocatalyst. Int J Eng Trans A. 2021;34:721–7. https://doi.org/10.5829/ije.2021.34.03c.17.
37. Ur Rahman Z, Shah U, Alam A, Shah Z, Shaheen K, Bahadar Khan S, Ali Khan S. Photocatalytic degradation of cefixime using CuO-NiO nanocomposite photocatalyst. Inorg Chem Commun. 2023. https://doi.org/10.1016/j.inoche.2022.110312.
38. Bakre PV, Kamat DP, Mandrekar KS, Tilve SG, Ghosh NN. CuO-NiO-TiO2 bimetallic nanocomposites for catalytic applications. Molecular Catalysis. 2020. https://doi.org/10.1016/j.mcat.2020.111193.
39. do Couto-Pessanha E, Paiva VM, Mori TJA, Soler L, Canabarro B, Jardim P, D'Elia E, Llorca J, Marinkovic BA Mechanochemical approach towards optimized Ni2+ spin configuration in NiO/TiO2 heterojunction with enhanced solar-driven H2 photoproduction. Int J Hydrogen Energy 2024;80:528–541. https://doi.org/10.1016/j.ijhydene.2024.07.037
40. Fawzi T, Huang PC, Kim J, Hung WH, Lin WC, Lee H. Efficient and economically affordable TiO2 nanotube-based ternary photocatalysts for CO2 conversion boosted by NiO nanoparticles and carbon quantum dots. Electrochim Acta. 2024. https://doi.org/10.1016/j.electacta.2024.144587.
41. Kumar Sahoo SPA, Ray K, Pandey D. Addition of CuO to form CuO/TiO2 and CuO/ZnO heterojunctions for photocatalytic CO2 conversion to methanol. Chem Phys Lett. 2024. https://doi.org/10.1016/j.cplett.2024.141678.
42. Tian X, Dong Y, Zahid M. One-pot synthesis of CuO/TiO2 nanocomposites for improved photocatalytic hydrogenation of 4-nitrophenol to 4-aminophenol under direct sunlight. J Chin Chem Soc. 2023;70:848–56. https://doi.org/10.1002/jccs.202300090.
43. Villachica-Llamosas JG, Ruiz-Aguirre A, Colón G, Peral J, Malato S. H2 production based on a ternary mixture of commercial CuO-NiO-TiO2 in a solar pilot plant. Catal Today. 2024. https://doi.org/10.1016/j.cattod.2024.114608.
44. Cai M, He C, Yu H, Shui A. Fabrication of the ternary dual S-scheme ZnO/ZnS/In2S3 heterojunction for enhancing pollutant photodegradation. Appl Surf Sci. 2024. https://doi.org/10.1016/j.apsusc.2023.159284.
45. Schumacher L, Marschall R, Recent advances in semiconductor heterojunctions and Z-schemes for photocatalytic hydrogen generation. Top Curr Chem 380 (2022)
46. Gusmão C, Palharim PH, Diniz LA, de Assis GC, de Carvalho e ST, Ramos B, Teixeira ACSC. Advances in fluidized bed photocatalysis: bridging gaps standardizing metrics, and shaping sustainable solutions for environmental challenges. Ind Eng Chem Res. 2024;63:14967–82.
47. Park JH, Seo YS, Kim HS, Kim IK. Photodegradation of benzene, toluene, ethylbenzene and xylene by fluidized bed gaseous reactor with TiO2/SiO2 photocatalysts. Korean J Chem Eng. 2011;28:1693–7. https://doi.org/10.1007/s11814-011-0021-9.
48. Sannino D, Ciambelli P, Palma V, Vaiano V, Mazzei RS. Improved performances of a fluidized bed photoreactor by a microscale illumination system. Int J Photoenergy. 2009. https://doi.org/10.1155/2009/709365.
49. Morante N, Tammaro O, Albarano L, De Guglielmo L, Oliva N, Sacco O, Mancuso A, Castellino M, Sannino D, Femia N, Lofrano G, Libralato G, Esposito S, Vaiano V. Influence of visible light LEDs modulation techniques on photocatalytic degradation of ceftriaxone in a flat plate reactor. Chem Eng J. 2024. https://doi.org/10.1016/j.cej.2024.149175.

50. Morante N, Tammaro O, Monzillo K, Sannino D, Battiato A, Vittone E, Castellino M, Esposito S, Vaiano V. Unraveling the role of CuO in CuxO/TiO2 photocatalyst for the direct propylene epoxidation with O2 in a fluidized bed reactor. Chemsuschem. 2024. https://doi.org/10.1002/cssc.202401546.
51. Makuła P, Pacia M, Macyk W. How to correctly determine the band gap energy of modified semiconductor photocatalysts based on UV-Vis spectra. J Phys Chem Lett. 2018;9:6814–7.
52. Ullah F, Ghani U, Mohamed Saheed MS. A PN-type CuO@TiO2 nanorods heterojunction for efficient PEC water splitting: DFT model and experimental investigation on the effect of calcination temperature. Int J Hydrogen Energy. 2023;48:39866–84. https://doi.org/10.1016/j.ijhydene.2023.07.159.
53. Mannaa MA, Qasim KF, Alshorifi FT, El-Bahy SM, Salama RS. Role of NiO nanoparticles in enhancing structure properties of TiO2and Its applications in photodegradation and hydrogen evolution. ACS Omega. 2021;6:30386–400. https://doi.org/10.1021/acsomega.1c03693.
54. Sagadevan S, Pal K, Chowdhury ZZ. Fabrication of CuO nanoparticles for structural, optical and dielectric analysis using chemical precipitation method. J Mater Sci: Mater Electron. 2017;28:12591–7. https://doi.org/10.1007/s10854-017-7083-3.
55. Ciambelli P, Sannino D, Palma V, Vaiano V. The effect of sulphate doping on nanosized TiO2 and MoO x /TiO2 catalysts in cyclohexane photooxidative dehydrogenation. Int J Photoenergy. 2008. https://doi.org/10.1155/2008/258631.
56. Sannino D, Vaiano V, Ciambelli P. Innovative structured VOx/TiO2 photocatalysts supported on phosphors for the selective photocatalytic oxidation of ethanol to acetaldehyde. Catal Today. 2013;205:159–67. https://doi.org/10.1016/j.cattod.2012.07.038.
57. Sannino D, Vaiano V, Ciambelli P, Carotenuto G, Di Serio M, Santacesaria E. Enhanced performances of grafted VOx on titania/silica for the selective photocatalytic oxidation of ethanol to acetaldehyde. Catal Today. 2013;209:159–63. https://doi.org/10.1016/j.cattod.2012.12.009.
58. Morante N, Tammaro O, Monzillo K, Sannino D, Battiato A, Vittone E, Castellino M, Esposito S, Vaiano V. Unraveling the role of CuO in Cu_xO/TiO_2 photocatalyst for the Direct Propylene epoxidation With O_2 in a fluidized bed reactor. Chemsuschem. 2024. https://doi.org/10.1002/cssc.202401546.
59. Moreno I, Avendaño-Alejo M, Tzonchev RI. Designing light-emitting diode arrays for uniform near-field irradiance. Appl Opt. 2006;45:2265–72. https://doi.org/10.1364/AO.45.002265.
60. Eisenberg GM. Colorimetric determination of hydrogen peroxide optimum quantity of test reagent for maximum color development
61. Khemthong P, Photai P, Grisdanurak N. Structural properties of CuO/TiO2 nanorod in relation to their catalytic activity for simultaneous hydrogen production under solar light. Int J Hydrogen Energy. 2013;38:15992–6001. https://doi.org/10.1016/j.ijhydene.2013.10.065.
62. Nishikiori H, Harata N, Yamaguchi S, Ishikawa T, Kondo H, Kikuchi A, Yamakami T, Teshima K. Formation of CuO on TiO2 surface using its photocatalytic activity. Catalysts. 2019. https://doi.org/10.3390/catal9040383.
63. El-Deen SS, Hashem AM, Abdel Ghany AE, Indris S, Ehrenberg H, Mauger A, Julien CM. Anatase TiO2 nanoparticles for lithium-ion batteries. Ionics (Kiel). 2018;24:2925–34. https://doi.org/10.1007/s11581-017-2425-y.
64. Muthamilarasu A, Sivakumar S, Divya G, Sivakumar M, Sakthi D. NiO/CuO/TiO 2 ternary composites: development, physicochemical characterization and photocatalytic degradation study over reactive orange 30 solutions under solar light irradiation. Adv Mater Sci. 2022;22:36–54. https://doi.org/10.2478/adms-2022-0003.
65. Nguyen TH, Nguyen TL, Ung TDT, Nguyen QL. Synthesis and characterization of nano-CuO and CuO/TiO2 photocatalysts. Adv Nat Sci: Nanosci Nanotechnol. 2013. https://doi.org/10.1088/2043-6262/4/2/025002.
66. Terlemezoglu M, Surucu O, Isik M, Gasanly NM, Parlak M. Temperature-dependent optical characteristics of sputtered NiO thin films. Appl Phys A Mater Sci Process. 2022. https://doi.org/10.1007/s00339-021-05197-y.
67. Pansri S, Supruangnet R, Nakajima H, Rattanasuporn S, Noothongkaew S. Band offset determination of p-NiO/n-TiO2 heterojunctions for applications in high-performance UV photodetectors. J Mater Sci. 2020;55:4332–44. https://doi.org/10.1007/s10853-019-04305-x.
68. Sim LC, Ng KW, Ibrahim S, Saravanan P. Preparation of improved p-n junction NiO/TiO2 nanotubes for solar-energy-driven light photocatalysis. Int J Photoenergy. 2013. https://doi.org/10.1155/2013/659013.
69. Abirami S, Kumar E. A review on metal oxide-doped polyaniline nanocomposites. J Mater Sci. 2024;59:14141–71.
70. Shi Q, Ping G, Wang X, Xu H, Li J, Cui J, Abroshan H, Ding H, Li G. CuO/TiO 2 heterojunction composites: an efficient photocatalyst for selective oxidation of methanol to methyl formate. J Mater Chem A Mater. 2019;7:2253–60. https://doi.org/10.1039/c8ta09439j.
71. Drobná H, Meinhardová V, Dubnová L, Kozumplíková K, Reli M, Kočí K, Čapek L. Partially reduced Ni-NiO-TiO2 photocatalysts for hydrogen production from methanol-water solution. Catalysts. 2023. https://doi.org/10.3390/catal13020293.
72. Jubu PR, Obaseki OS, Ajayi DI, Danladi E, Chahrour KM, Muhammad A, Landi S, Igbawua T, Chahul HF, Yam FK. Considerations about the determination of optical bandgap from diffuse reflectance spectroscopy using the tauc plot. J Optics (India). 2024. https://doi.org/10.1007/s12596-024-01741-0.
73. Uddin MT, Nicolas Y, Olivier C, Jaegermann W, Rockstroh N, Junge H, Toupance T. Band alignment investigations of heterostructure NiO/TiO2 nanomaterials used as efficient heterojunction earth-abundant metal oxide photocatalysts for hydrogen production. Phys Chem Chem Phys. 2017;19:19279–88. https://doi.org/10.1039/c7cp01300k.
74. Ku Y, Lee PC, Luong GK. Photocatalytic reduction of gaseous carbon dioxide over NiO/TiO2 under UV light illumination. J Taiwan Inst Chem Eng. 2021;125:291–6. https://doi.org/10.1016/j.jtice.2021.06.036.
75. Yang D, Du F, Ren Y, Kang T, Hu P, Teng F, Fan H. A high-performance NiO/TiO2UV photodetector: the influence of the NiO layer position. J Mater Chem C Mater. 2021;9:14146–53. https://doi.org/10.1039/d1tc02687a.
76. Castañeda C, Martínez JJ, Santos L, Rojas H, Osman SM, Gómez R, Luque R. Caffeine photocatalytic degradation using composites of NiO/TiO2–F and CuO/TiO2–F under UV irradiation. Chemosphere. 2022. https://doi.org/10.1016/j.chemosphere.2021.132506.
77. Li L, Chen X, Quan X, Qiu F, Zhang X. Synthesis of CuOx/TiO2 photocatalysts with enhanced photocatalytic performance. ACS Omega. 2023;8:2723–32. https://doi.org/10.1021/ACSOMEGA.2C07364.
78. Abdullah SA, Sahdan MZ, Nafarizal N, Saim H, Bakri AS, Cik Rohaida CH, Adriyanto F, Sari Y. Photoluminescence study of trap-state defect on TiO2 thin films at different substrate temperature via RF magnetron sputtering. In: Journal of Physics: Conference Series. Institute of Physics Publishing (2018)

79. Sun M, Chen Z, Yu J. Highly efficient visible light induced photoelectrochemical anticorrosion for 304 SS by Ni-doped TiO2. Electrochim Acta. 2013;109:13–9. https://doi.org/10.1016/j.electacta.2013.07.121.
80. Lamouchi W, Ben SS, Saadallah F, Bouaicha M. Nickel doping induced amorphization of brookite TiO2: photoluminescence enhancement. Optik (Stuttg). 2021. https://doi.org/10.1016/j.ijleo.2020.166123.
81. Yamakata A, Kawaguchi M, Murachi R, Okawa M, Kamiya I. Dynamics of photogenerated charge carriers on Ni- and Ta-doped SrTiO3 photocatalysts studied by time-resolved absorption and emission spectroscopy. J Phys Chem C. 2016;120:7997–8004. https://doi.org/10.1021/acs.jpcc.6b01494.
82. Wang X, Zhou P, Zhou Q, Zhang Q, Ning H, Wu M, Wu W. Tandem photocatalytic production of H2O2 and propylene oxide on 5-Bromoisatin modified carbon nitride. Chem Eng J. 2023. https://doi.org/10.1016/j.cej.2023.146488.
83. Lewis RJ, Hutchings GJ. Selective oxidation using in situ-generated hydrogen peroxide. Acc Chem Res. 2024;57:106–19. https://doi.org/10.1021/acs.accounts.3c00581.
84. Alvear M, Orabona F, Eränen K, Lehtonen J, Rautiainen S, Di Serio M, Russo V, Salmi T. Epoxidation of light olefin mixtures with hydrogen peroxide on TS-1 in a laboratory-scale trickle bed reactor: transient experimental study and mathematical modelling. Chem Eng Sci. 2023;269:118467.
85. Thambiliyagodage C, Mirihana S. Photocatalytic activity of Fe and Cu co-doped TiO2 nanoparticles under visible light. J Solgel Sci Technol. 2021;99:109–21. https://doi.org/10.1007/s10971-021-05556-4.
86. Nguyen PH, Pham MT, Nguyen HQ, Cao TM, Van PV. Boosting visible-light-driven photocatalysis of nitrogen oxide degradation by Mott-Schottky Pd/TiO2 heterojunctions. Sep Purif Technol. 2025. https://doi.org/10.1016/j.seppur.2024.129012.
87. Tateishi I, Furukawa M, Katsumata H, Kaneco S. Effective utilization of sulfur wastewater by photocatalytic system using B/CuO/ZnO. Separations. 2024. https://doi.org/10.3390/separations11010019.
88. Deitermann M, Haver Y, Mei BT, Muhler M. The influence of the reaction conditions on the photocatalytic gas-phase conversion of methanol with water vapor over Pt/SrTiO3 in a continuously operated flow reactor. Adv Sustain Syst. 2024. https://doi.org/10.1002/adsu.202300329.
89. Herrmann JM. Heterogeneous photocatalysis: state of the art and present applications. Top Catal. 2005;34:49–65. https://doi.org/10.1007/s11244-005-3788-2.
90. Du W, Zhang Z, Wang J, Song N, Duan X, Zhou X. Kinetic insights into reaction pathways of acrolein formation in propylene epoxidation by H2 and O2 over Au/TS-1 catalyst. Chem Eng J. 2024. https://doi.org/10.1016/j.cej.2024.150512.
91. Ravi P, Navakoteswara Rao V, Shankar MV, Sathish M. CuO@NiO core-shell nanoparticles decorated anatase TiO2 nanospheres for enhanced photocatalytic hydrogen production. Int J Hydrogen Energy. 2020;45:7517–29. https://doi.org/10.1016/j.ijhydene.2019.05.020.
92. Feiner1 A-S, Mcevoy AJ The Nernst Equation
93. Janczarek M, Kowalska E. On the origin of enhanced photocatalytic activity of copper-modified titania in the oxidative reaction systems. Catalysts 7 (2017)
94. Gao T, Li TT, Liao X, Lin JH, Shiu BC, Lou CW. Construction of Cu2O/TiO2heterojunction photoelectrodes for photoelectrochemical determination of glucose. J Market Res. 2022;21:798–809. https://doi.org/10.1016/j.jmrt.2022.09.043.
95. Gnanaguru MVL, Parida VK, Ghangrekar MM, Gupta AK, Chowdhury S. Insights into the performance of binary heterojunction photocatalysts for degradation of refractory pollutants. Environ Sci Pollut Res. 2024;31:11349–70.
96. Ou M, Zhong Q, Zhang S, Yu L. Ultrasound assisted synthesis of heterogeneous g-C3N4/BiVO4 composites and their visible-light-induced photocatalytic oxidation of NO in gas phase. J Alloys Compd. 2015;626:401–9. https://doi.org/10.1016/j.jallcom.2014.11.148.
97. Koppenol WH, Stanbury DM, Bounds PL. Electrode potentials of partially reduced oxygen species, from dioxygen to water. Free Radic Biol Med. 2010;49:317–22.
98. Dutta A, Lazaridis T. Classical models of hydroxide for proton hopping simulations. J Phys Chem B. 2024. https://doi.org/10.1021/acs.jpcb.4c05499.
99. Bolton JR, Bircher KG, Tumas W, Tolman CA (2001) Figures-of-merit for the technical development and application of advanced oxidation technologies for both electric-and solar-driven systems † (IUPAC Technical Report)
100. Nguyen V-H, Lin SD, Wu JC-S. Synergetic photo-epoxidation of propylene over VTi/MCM-41 mesoporous photocatalysts. J Catal. 2015;331:217–27.
101. Amano F, Tanaka T. Modification of photocatalytic center for photo-epoxidation of propylene by rubidium ion addition to V2O5/SiO2. Catal Commun. 2005;6:269–73. https://doi.org/10.1016/j.catcom.2005.01.007.
102. Pierre P, Marie HJ, Jean D, Noelle MM. Photocatalytic oxidation of propene over various oxides at 320 K Selectivity. J Phys Chem. 1979;83:3122–6. https://doi.org/10.1021/j100487a012.
103. Murcia-López S, Vaiano V, Sannino D, Hidalgo MC, Navío JA. Photocatalytic propylene epoxidation on Bi2WO6-based photocatalysts. Res Chem Intermed. 2015;41:4199–212. https://doi.org/10.1007/s11164-013-1523-3.

Publisher's Note